ARTICLES
https://doi.org/10.1038/s41588-021-00888-x

nature genetics

Check for updates

# Orphan CpG islands amplify poised enhancer regulatory activity and determine target gene responsiveness

Tomas Pachano[1,2], Víctor Sánchez-Gaya[2], Thais Ealo[2], Maria Mariner-Faulí[2], Tore Bleckwehl[1], Helena G. Asenjo[3,4,5], Patricia Respuela[2], Sara Cruz-Molina[6], María Muñoz-San Martín[2], Endika Haro[2], Wilfred F. J. van IJcken[7], David Landeira[3,4,5] and Alvaro Rada-Iglesias[1,2,8] ✉

**CpG islands (CGIs) represent a widespread feature of vertebrate genomes, being associated with ~70% of all gene promoters. CGIs control transcription initiation by conferring nearby promoters with unique chromatin properties. In addition, there are thousands of distal or orphan CGIs (oCGIs) whose functional relevance is barely known. Here we show that oCGIs are an essential component of poised enhancers that augment their long-range regulatory activity and control the responsiveness of their target genes. Using a knock-in strategy in mouse embryonic stem cells, we introduced poised enhancers with or without oCGIs within topologically associating domains harboring genes with different types of promoters. Analysis of the resulting cell lines revealed that oCGIs act as tethering elements that promote the physical and functional communication between poised enhancers and distally located genes, particularly those with large CGI clusters in their promoters. Therefore, by acting as genetic determinants of gene–enhancer compatibility, CGIs can contribute to gene expression control under both physiological and potentially pathological conditions.**

Enhancers are a heterogeneous group of distal *cis*-regulatory elements containing clusters of transcription factor binding sites (TFBSs) that control gene expression in a distance- and orientation-independent manner[1]. The regulatory properties of enhancers have been mostly investigated using transgenic reporter assays[2] in which enhancer activity is evaluated by measuring the capacity to activate transcription of a reporter gene from a minimal promoter. In these assays, the investigated sequences are placed at short distances from the reporter genes, using a limited set of minimal promoters. On the other hand, insulators prevent enhancers from ectopically activating nontarget genes[3]. In vertebrates, insulators are typically bound by CTCF, which, together with Cohesin, can form long-range chromatin loops that demarcate the boundaries of regulatory domains and limit enhancer activity[4]. Current models of enhancer function implicitly assume that enhancers and genes can effectively communicate with each other, regardless of distance or sequence composition, as far as they are located within the same regulatory domain[3]. However, recent studies show that the disruption of regulatory domains does not always lead to changes in gene expression or enhancer–gene communication[5–9]. Similarly, enhancers and their developmental target genes can reside within the same regulatory domains together with 'bystander' genes that are not responsive to the enhancers[10]. Therefore, additional factors, such as the type of core-promoter elements[11,12], contribute to enhancer responsiveness. However, it is currently unknown whether other genetic factors (for example, distance or enhancer sequence composition) can also contribute to such responsiveness, which is essential to understand the pathological consequences of human structural variation[13].

We previously showed that poised enhancers (PEs) control the induction of major neural genes upon mouse embryonic stem cell (ESC) differentiation[14]. Before becoming active in anterior neural progenitors (AntNPCs), PEs are already bookmarked in ESCs with unique chromatin and topological features, including binding by polycomb-group protein complexes (PcG) and preformed contacts with their target genes[14,15]. PEs have a distinctive genetic composition that includes not only clusters of TFBSs but also nearby CGIs[14]. CGIs are a prevalent feature of vertebrate gene promoters, providing them with a permissive chromatin state that facilitates transcription initiation[16]. However, only half of the CGIs found in the mouse and human genomes are associated with promoters (pCGIs)[16,17], while the other half, known as oCGIs, remain poorly studied. oCGIs have been proposed to act as alternative gene promoters[18] or highly active enhancers with limited tissue specificity[17,19,20]. Nevertheless, the mechanisms whereby oCGIs might contribute to transcriptional regulation remain unknown. Here we show that oCGIs act as long-range potentiators of PEs, enabling the functional communication between PEs and developmental genes with CpG-rich promoters. Therefore, our work uncovers CGIs as major determinants of enhancer–gene compatibility and provides important insights into how gene expression programs are specifically and precisely deployed during development.

[1]Center for Molecular Medicine Cologne (CMMC), University of Cologne, Cologne, Germany. [2]Institute of Biomedicine and Biotechnology of Cantabria (IBBTEC), CSIC/Universidad de Cantabria/SODERCAN, Santander, Spain. [3]Centre for Genomics and Oncological Research (GENYO), Granada, Spain. [4]Department of Biochemistry and Molecular Biology II, Faculty of Pharmacy, University of Granada, Granada, Spain. [5]Instituto de Investigación Biosanitaria ibs.GRANADA, Hospital Virgen de las Nieves, Granada, Spain. [6]Max Planck Institute for Molecular Biomedicine, Muenster, Germany. [7]Center for Biomics, Erasmus University Medical Center, Rotterdam, the Netherlands. [8]Cologne Excellence Cluster for Cellular Stress Responses in Aging-Associated Diseases (CECAD), University of Cologne, Cologne, Germany. ✉e-mail: alvaro.rada@unican.es

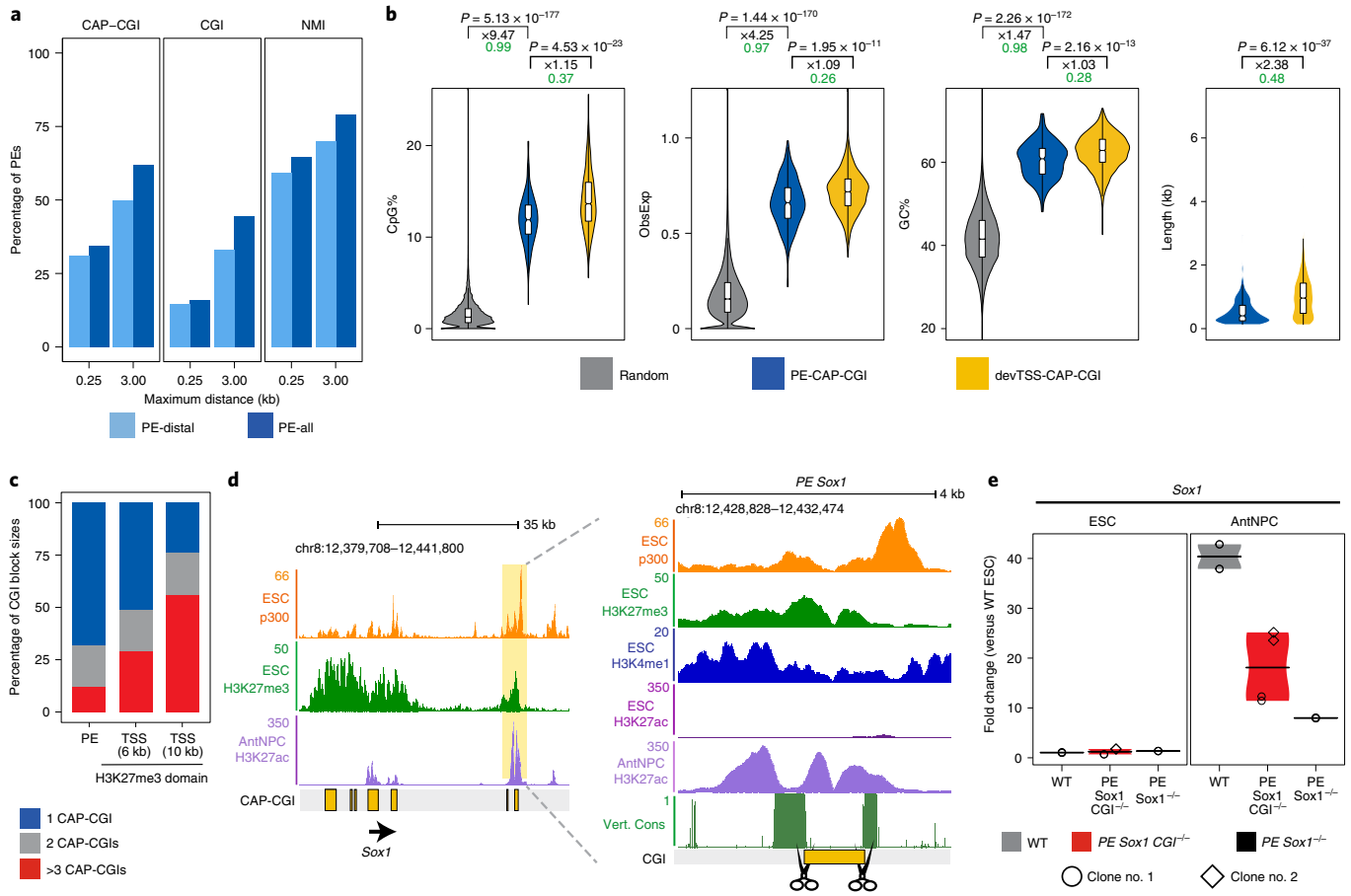


**Fig. 1 | Genetic properties and functional relevance of oCGIs associated with PEs. a**, Percentage of PEs within the indicated maximum distances (0.25 kb or 3.00 kb) of a CGI identified by CAP-seq[18] (left), an NMI[21] (middle) or a computationally defined CGI (right). **b**, Comparison of the CpG%, observed/expected CpG ratio, GC% and sequence length between random regions ($n = 436{,}000$), CAP-CGIs associated with *PE-distal* (PE-CAP-CGI; $n = 276$) and CAP-CGIs associated with the TSS of developmental genes (devTSS-CAP-CGI; $n = 1{,}926$) (Methods). *P* values were calculated using unpaired two-sided Wilcoxon tests with Bonferroni correction for multiple testing; black numbers indicate median fold-changes; green numbers indicate non-negligible Cliff's delta effect sizes. The center line of the violin plot represents the median, the boxes encompass the interquartile range and the whiskers extend to the minimum and maximum. **c**, Percentage of CAP-CGI block sizes (1, 2 or ≥3 CAP-CGIs) associated with *PE-distal* ($n = 253$) or the TSS of developmental genes (*devTSS*; $n = 1{,}522$ with at least one CAP-CGI in <3 kb). The *devTSS*s were classified in two groups based on the length of the H3K27me3 domains associated with them (>6 kb ($n = 1{,}522$) and >10 kb ($n = 599$)). **d**, Left panel, ChIP-seq data[14] from ESCs (p300 and H3K27me3) and AntNPCs (H3K27ac) at the *Sox1* locus. The *PE Sox1(+35)* is highlighted in yellow. Right panel, close-up view of the *PE Sox1(+35)* with additional epigenomic and genomic data, including a computationally defined CGI. Vert. Cons, vertebrate PhastCons. **e**, *Sox1* expression was investigated by RT-qPCR in cells that were WT, homozygous for a deletion of the *PE Sox1(+35) CGI* (*PE Sox1 CGI*$^{-/-}$) or homozygous for a deletion of the complete *PE Sox1(+35)*[14] (*PE Sox1*$^{-/-}$). $N = 2$ independent *PE Sox1 CGI*$^{-/-}$ ESC clones (circles and diamonds) and $n = 1$ *PE Sox1*$^{-/-}$ clone were studied. For each ESC clonal line, $n = 2$ replicates of the AntNPC differentiation were performed. Expression values were normalized to two housekeeping genes (*Eef1a* and *Hprt*) and are presented as fold-changes with respect to WT ESCs. The colored area of the violin plot represents the expression values distribution and the center line represents the median. $n = 1$ independent biological replicate of this experiment is shown in Extended Data Fig. 1f. ObsExp, observed to expected CpG ratio.

## Results

**Genetic properties of PE-associated oCGIs.** PEs identified in mouse ESCs are commonly located in proximity to computationally predicted CGIs[14]. However, computational models underestimate the abundance of CGIs, especially those distally located from transcription start sites (TSSs)[21]. Using biochemically identified CGIs ((1) CGIs identified by CXXC affinity purification and deep sequencing (CAP–seq) (that is, CAP-CGIs)[18] and (2) nonmethylated islands (NMIs)[21]), we found that ~60–80% of PEs are located within 3 kilobases (kb) of a CAP-CGI or an NMI, respectively (Fig. 1a). In comparison with the CAP-CGIs located in proximity of the TSSs of developmental genes, those associated with PEs were shorter and had lower CpG density (Fig. 1b). Moreover, PEs tend to be associated with single CAP-CGIs, whereas developmental gene promoters frequently contain clusters of two or more CAP-CGIs[22] (Fig. 1c and Extended Data Fig. 1a). Here we use the term oCGI regardless of whether these sequences are identified computationally or experimentally, although many of the PE oCGIs display lower GC content and CpG ratios than the classically defined CGIs (Fig. 1b).

pCGIs serve as recruitment platforms for proteins that can modify chromatin (for example, PcG, TET1)[23,24]. Consequently, pCGIs are hypomethylated and enriched in H3K27me3 (refs. [14,15]). Analysis of publicly available data[14,25–28] showed that PEs associated with CAP-CGIs are also hypomethylated and more enriched in H3K27me3 than PEs or active enhancers (AE) not linked to CAP-CGIs (Extended Data Fig. 1b,c). Therefore, PEs are pervasively found in proximity of CGIs, which in turn might endow them with unique chromatin features.

**oCGIs are necessary for PE regulatory function.** To start evaluating the regulatory role of oCGIs in the context of PEs, we generated mouse ESC lines with a homozygous deletion of the oCGI associated with *PE Sox1(+35)*, a PE that controls the expression of *Sox1* in neural progenitors[14] (Fig. 1d and Extended Data Fig. 1d). The oCGI deletion severely reduced H3K27me3 levels around *PE Sox1(+35)* in ESCs (Extended Data Fig. 1e). Next, we measured *Sox1* expression in wild-type (WT), *PE Sox1(+35)CGI*$^{-/-}$ and *PE Sox1(+35)*$^{-/-}$ ESCs as well as upon their differentiation into AntNPCs. In ESCs, neither the deletion of the oCGI nor of the whole *PE Sox1(+35)* affected *Sox1* expression (Fig. 1e and Extended Data Fig. 1f). However, in AntNPCs the oCGI deletion reduced *Sox1* expression by >2-fold (Fig. 1e and Extended Data Fig. 1f), thus suggesting that oCGIs might positively influence the *cis*-activation capacity of PEs[14].

**Dissection of PE regulatory logic by genetic engineering.** The functional assessment of PE oCGIs using loss-of-function approaches has certain limitations: (1) oCGIs can be difficult to delete individually, as they frequently overlap with nearby TFBSs (Extended Data Fig. 2a); (2) PE target genes typically display complex regulatory landscapes in which multiple enhancers control gene expression[29], thus potentially masking the regulatory function of individual oCGIs; and (3) the loss of CGI-bound proteins (for example, PcG) can elicit global molecular changes that indirectly alter PE loci.

To systematically dissect the contribution of oCGIs to the regulatory function of PEs, we designed a genetic engineering approach to generate ESCs in which the components of selected PEs are modularly inserted (that is, TFBS, oCGI or TFBS + oCGI) into a fixed genomic location (Fig. 2a). We reasoned that by selecting insertion sites located within topologically associating domains (TADs) containing developmental genes not expressed in ESCs or AntNPCs and, thus, without AEs in these cell types, any changes in the expression of the selected genes could be attributed solely to the inserted PE sequences. To implement this approach, we initially inserted the *PE Sox1(+35)* components (that is, *PE Sox1(+35)TFBS*, *PE Sox1(+35)CGI* or *PE Sox1(+35)TFBS+CGI*) approximately 100 kb downstream of *Gata6* (Fig. 2a), a gene with multiple CGIs around its promoter region and weakly expressed in both ESCs and AntNPCs. The selected insertion site was not conserved and was not close to any CTCF binding site (CBS), thus minimizing the risk of disrupting any regulatory element. Using this strategy, we established two homozygous ESC clones for each of the *PE Sox1(+35)* inserts described above (Extended Data Fig. 2b). Next, we measured *Gata6* expression in the previous ESC lines and upon their differentiation into AntNPCs. In ESCs none of the engineered *PE Sox1(+35)* combinations affected *Gata6* expression (Fig. 2b and Extended Data Fig. 2c). Strikingly, upon differentiation into AntNPCs, *Gata6* was strongly induced in cells with the *TFBS + CGI* insertion (~50-fold versus WT). In contrast, cells with the *TFBS* displayed considerably milder *Gata6* induction (~7-fold versus WT), while the *CGI* had no effect on *Gata6* expression (Fig. 2b and Extended Data Fig. 2c).

**oCGIs amplify PE regulatory activity.** To evaluate whether the previous observations could be generalized, we generated two additional groups of transgenic ESC lines: (1) *PE Sox1(+35)* components were inserted within the *Foxa2*-TAD (~100 kb downstream of *Foxa2* TSS, which contains several CGIs and is inactive in ESCs and AntNPCs); (2) *PE Wnt8b(+21)* (ref. [14]) components were inserted within the *Gata6*-TAD (~100 kb downstream of *Gata6*-TSS) (Extended Data Fig. 2d–g). Importantly, the *TFBS + CGI* inserts were able to strongly induce gene expression in AntNPCs (Fig. 2c,d and Extended Data Fig. 2h,i), while the *TFBS* or the *oCGI* alone led to either no or minor gene inductions, respectively (Fig. 2c,d and Extended Data Fig. 2h,i).

Next, we investigated whether the boosting capacity of the oCGIs could be attributed to other types of regulatory information beyond their CpG-richness (for example, TFBSs). In silico motif analyses using as input either the CAP-CGIs or the TFBS/p300 peaks from PEs in which these elements do not overlap (Fig. 2e) showed that p300 peaks, but not CAP-CGIs, were strongly enriched in binding motifs for pluripotency transcription factors (TFs)[14] (for example, OCT4, SOX2, NANOG). Similarly, differential motif analyses revealed that CpG-rich motifs were strongly overrepresented among PEs compared with AEs (Extended Data Fig. 3a)[14]. CGIs can serve as recruitment platforms for proteins containing ZF-CxxC domains (for example, KDM2B, TET1)[16,30], which could contribute to the unique chromatin features of PEs (Extended Data Fig. 1b,c). Analysis of KDM2B and TET1 chromatin immunoprecipitation sequencing (ChIP–seq) data generated in ESCs[31,32] showed that the binding of these proteins to PEs was positively correlated with the presence of nearby CAP-CGIs (Extended Data Fig. 3b). Next, we designed an artificial CGI (aCGI; Methods) and inserted it alone or together with the *PE Sox1(+35)TFBS* at the *Gata6*-TAD (Extended Data Fig. 4a,b,d). Notably, the *TFBS + aCGI* considerably increased *Gata6* expression in AntNPCs compared with the *TFBS* (Fig. 2f and Extended Data Fig. 4c), whereas the insertion of the aCGI alone did not alter *Gata6* expression (Extended Data Fig. 4e). Although we cannot completely dismiss that some oCGIs contain relevant binding sites for tissue-specific TFs, our results indicate that the CpG-richness of the oCGIs is important to increase the regulatory activity of PEs.

The boosting properties of oCGIs might be attributed to a premature induction of the target gene, an increase in the number of cells in which the target gene becomes induced and/or an increase in the expression levels within individual cells. To address this, we focused on those cell lines containing the different *PE Sox1(+35)* components inserted within the *Gata6*-TAD. Upon differentiation

**Fig. 2 | Modular engineering of PEs reveals major regulatory functions for oCGIs. a**, Strategy to insert the *PE Sox1(+35)* components into the *Gata6*-TAD. Left, epigenomic and genetic features of the *PE Sox1(+35)*. The oCGI is not evolutionarily conserved. Middle, the three combinations of *PE Sox1(+35)* modules inserted into the *Gata6*-TAD. Right, TAD in which *Gata6* is located (that is, *Gata6*-TAD)[80,81]. The red triangle indicates the integration site of the *PE Sox1(+35)* modules approximately 100 kb downstream of *Gata6*. **b**–**d**,**f**, The expression of *Gata6* (**b**, **d** and **f**), *Foxa2* (**c**), *Sox1* (**b**, **c** and **f**) and *Wnt8b* (**d**) was measured by RT-qPCR in ESCs and AntNPCs that were either WT or homozygous for the insertion of the different *PE Sox1(+35)* (**b**,**c**) or *PE Wnt8b(+21)* (**d**) modules. In **f**, the *PE Sox1(+35)TFBS* was inserted alone or in combination with an aCGI into the *Gata6*-TAD. For the cells with the PE insertions, $n = 2$ independent clonal cell lines (circles and diamonds) were studied in each case. For each cell line, $n = 2$ replicates of the AntNPC differentiation were performed. Expression values were normalized to two housekeeping genes (*Eef1a* and *Hprt*) and are presented as fold-changes with respect to WT ESCs. $N = 1$ independent biological replicate of these experiments is shown in Extended Data Fig. 2. In **b**–**d** and **f**, the expression differences between AntNPCs with the TFBS + CGI module and AntNPCs with the other PE modules were calculated using two-sided nonpaired *t*-tests (***fold-change > 2 and $P < 0.0001$; **fold-change > 2 and $P < 0.001$; *fold-change > 2 and $P < 0.05$; NS, not significant; fold-change < 2 or $P > 0.05$). The colored area of the violin plot represents the expression values distribution and the center line represents the median. **e**, TF motif analyses using *Homer*[82] and *SeqPos*[83] for PEs with a CAP-CGI within less than 3 kb and that do not overlap with the p300 peaks defining the PEs[14]. Motif analyses were performed separately for the CAP-CGIs and the p300 peaks. n/a, not available. **g**, Immunofluorescence assays for GATA6 and SOX1 in WT ESCs or AntNPCs that were either WT or homozygous for the insertion of the different *PE Sox1(+35)* modules in the *Gata6*-TAD. Scale bar, 100 µm.

of the *TFBS+CGI* ESCs into AntNPCs, *Gata6* did not become induced until day 4, thus matching the expression dynamics of *Sox1* (the endogenous target of *PE Sox1(+35)*) and arguing against premature gene induction due to the presence of the oCGI (Extended Data Fig. 5a). Next, we performed immunofluorescence assays to visualize GATA6 and SOX1 proteins in WT and *Gata6*-TAD cells. SOX1 became strongly and homogeneously induced in AntNPCs derived from all the evaluated cell lines[33] (Fig. 2g and Extended Data Fig. 5b–d). Notably, GATA6 was also induced in ~50% and ~60% of the AntNPCs derived from *TFBS+CGI* or *TFBS+aCGI* ESCs, respectively (Fig. 2g and Extended Data Fig. 5c,d). In contrast, the *TFBS* resulted in noisier and more heterogeneous GATA6 expression, while no GATA6 could be detected in cells having the *CGI* or *aCGI* alone. These results suggest that oCGIs increase the number

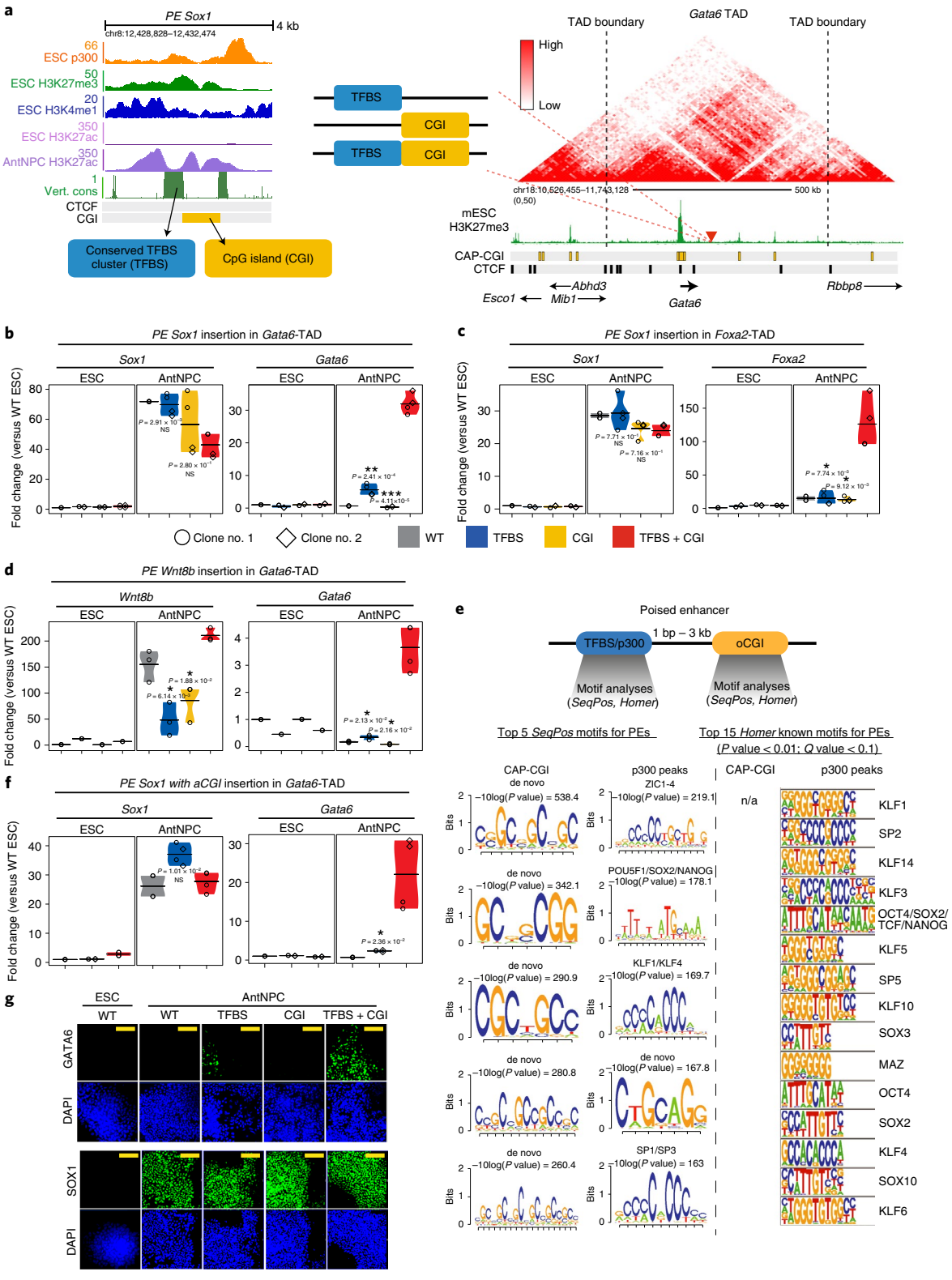

of cells in which the PE target genes get induced, thus potentially leading to high gene expression precision[34].

**oCGIs do not increase the local activation of PEs.** To investigate the mechanisms whereby oCGIs potentiate the regulatory function of PEs, we focused on the ESC lines in which the *PE Sox1(+35)* components were inserted within the *Gata6*-TAD. pCGIs are typically devoid of CpG methylation and display low nucleosomal density, which might provide a chromatin environment permissive for TF binding and transcription initiation[35,36]. Bisulfite sequencing experiments in *TFBS + CGI* and *TFBS* ESCs showed that the TFBS sequences acquired intermediate CpG methylation levels when inserted alone, while becoming completely unmethylated when combined with the oCGI (Fig. 3a and Extended Data Fig. 6a). In contrast, formaldehyde-assisted isolation of regulatory elements (FAIRE) assays showed that the oCGI only moderately increased chromatin accessibility whether inserted alone or in conjunction with the TFBS (Extended Data Fig. 6b). To simultaneously measure nucleosome occupancy and CpG methylation at the inserted TFBS with single-DNA-molecule resolution[37], we also performed nucleosome occupancy and methylome PCR (NOMe-PCR) assays. These experiments confirmed that oCGIs protect nearby TFBSs from CpG methylation without a major impact on chromatin accessibility (Extended Data Fig. 6c,d). Furthermore, upon differentiation into AntNPCs, the TFBSs got progressively demethylated in the *TFBS* cells (Fig. 3a and Extended Data Fig. 6a), suggesting that, even in the absence of an oCGI, TFs can access and activate PEs in AntNPCs[38]. To test this prediction, we performed chromatin immunoprecipitation coupled to quantitative PCR (ChIP–qPCR) experiments to measure p300 binding and H3K27ac levels, two major hallmarks of AEs[15], around the inserted *PE Sox1(+35)* constructs. Interestingly, in AntNPCs the PEs containing the *TFBS* alone or together with the *oCGI* became strongly and similarly enriched in H3K27ac and p300 (Fig. 3b). Therefore, the boosting capacity of the oCGIs cannot be simply attributed to their local chromatin effects.

**oCGIs increase PE–target gene communication.** Another distinctive hallmark of AEs is the production of short bidirectional transcripts termed enhancer RNAs (eRNAs)[39]. Remarkably, eRNA levels in AntNPCs were >20-fold higher around the *TFBS + CGI* insert in comparison with the *TFBS* alone (Fig. 3c). Moreover, upon AntNPC differentiation, the *TFBS + CGI* insert became highly enriched in RNA polymerase II (RNAP2) and Mediator (Fig. 3d). In contrast, the binding of these proteins to the *TFBS* and *CGI* inserts was either considerably weaker or undetectable, respectively (Fig. 3d). Similarly, the recruitment of RNAP2 and Mediator to the *Gata6* promoter was also stronger in AntNPCs with the *TFBS + CGI* insert (Fig. 3d).

In their inactive state, PEs are enriched in histone modifications (that is, H3K27me3 and H3K4me1) and protein complexes (for example, PcG) implicated in the establishment of long-range chromatin interactions[14,15,40,41]. Therefore, oCGIs could be implicated in the establishment of PEs' unique chromatin signature, facilitating the physical communication between PEs and their target genes. To investigate this possibility, we performed ChIP assays for H3K4me1, H3K4me3 and H3K27me3/PcG in the ESC lines containing the different *PE Sox1(+35)* components within the *Gata6*-TAD (Fig. 3e and Extended Data Fig. 6e,f). H3K4me1 was weakly enriched around the *PE Sox1(+35)* inserts containing the *TFBS* with or without the *oCGI*, while no enrichment was observed for the *oCGI* insert alone (Extended Data Fig. 6e). On the other hand, H3K4me3 was not enriched in any of the evaluated ESC lines (Extended Data Fig. 6e), indicating that oCGIs do not adopt the same chromatin state as pCGI. Most interestingly, H3K27me3, H2AK119ub and additional PcG subunits (that is, SUZ12, CBX7, PHC1 and RING1B) were strongly enriched around the *PE Sox1(+35)* inserts containing the *oCGI* (Fig. 3e,f and Extended Data Fig. 6f). Intriguingly, PRC1 recruitment (that is, CBX7, PHC1 and RING1B) was considerably stronger for the *TFBS + oCGI* insert than for the *oCGI* alone (Fig. 3f and Extended Data Fig. 6f).

Since PcGs can mediate long-range homotypic interactions between distal PcG-bound loci[40–45], we investigated the three-dimensional organization of the *Gata6* locus in our engineered ESC lines. Circular chromosome conformation capture coupled to sequencing (4C–seq) experiments using either the *Gata6* promoter or the *PE Sox1(+35)* insertion site as viewpoints revealed strong PE-*Gata6* contacts only in the *TFBS + CGI* cells (Fig. 3g). The lack of PE–gene contacts in cells with the *CGI* alone could be attributed to the weaker recruitment of PRC1 to the insert in these cells[46,47] (Extended Data Fig. 6f). Furthermore, the strong interactions between the *TFBS + CGI* insert and the *Gata6* promoter were also observed upon differentiation into AntNPCs (Extended Data Fig. 6g). Although the *TFBS* insert alone did not substantially contact with the *Gata6* promoter in AntNPCs (Extended Data Fig. 6g), *Gata6* was induced, albeit weakly, in these cells (Fig. 2b). This could be explained by the more transient and/or heterogeneous interactions between *Gata6* and the PE in the absence of the oCGI and/or by the capacity of enhancers to induce gene expression without getting into close proximity of their target genes[3,48,49]. Next, to evaluate whether oCGIs are important for PE–gene contacts in an endogenous genomic context, we performed 4C–seq experiments in the ESCs in which the oCGI associated with *PE Sox1(+35)* was deleted. Importantly, the deletion of this oCGI reduced the interactions between *Sox1* and *PE Sox1(+35)* (Fig. 3h).

Overall, our data suggest that oCGIs increase the functional communication between PEs and their target genes by bringing them into close spatial proximity.

**CpG-poor promoters do not show responsiveness to distal PEs.** Developmental genes, such as those regulated by PEs[14,15], contain

**Fig. 3 | Characterization of the epigenetic, topological and regulatory features of the *PE Sox1(+35)* modules engineered within the *Gata6*-TAD. a**, Bisulfite sequencing analyses in ESCs (day 0) and AntNPCs (day 5) differentiated from cell lines with the *PE Sox1(+35)TFBS* or *PE Sox1(+35)TFBS + CGI* modules inserted in the *Gata6*-TAD. DNA methylation levels were measured using a forward bisulfite primer upstream of the insertion site and a reverse primer inside the TFBS module (Methods). **b**, H3K27ac and p300 levels at the endogenous *PE Sox1(+35)*, the *Gata6*-TAD insertion site (P1 and P2 primer pairs) and the *Gata6* promoter were measured by ChIP–qPCR in ESCs (left) and AntNPCs (right) that were either WT (gray) or homozygous for the insertion of the different *PE Sox1(+35)* modules. ChIP–qPCR signals were normalized against two negative control regions (Supplementary Data 1). The bars display the mean of $n = 3$ technical replicates (black dots). **c**, eRNA levels at the endogenous *PE Sox1(+35)* and the *Gata6*-TAD insertion site (P1 and P2 primer pairs) were measured by RT–qPCR in ESCs (left) and AntNPCs (right) that were either WT (gray) or homozygous for the insertions of the different *PE Sox1(+35)* modules. Expression values were normalized to two housekeeping genes (*Eef1a* and *Hprt*) and are presented as fold-changes with respect to WT ESCs. The bars display the mean of $n = 3$ technical replicates (black dots). **d–f**, RNAP2 and MED1 (**d**), H3K27me3 (**e**) or SUZ12 and RING1B (**f**) levels were measured by ChIP–qPCR as described in **b**. **g**, 4C–seq experiments were performed using the *Gata6* promoter (upper panels) or the *Gata6*-TAD insertion site (lower panels) as viewpoints in ESCs that were either WT (gray) or homozygous for the insertions of the different *PE Sox1(+35)* modules. **h**, 4C–seq experiments were performed using the *PE Sox1(+35)* as a viewpoint in ESCs that were either WT or homozygous for the deletion of *PE Sox1(+35)* CGI (*PE Sox1 CGI*$^{-/-}$). The genomic locations of *PE Sox1(+35)* and *Sox1* are highlighted in gray. mCpG, methylated CpG; VP, viewpoint.

large CGI clusters around their promoters, whereas tissue-specific genes tend to have CpG-poor promoters[22]. PEs and their target genes could spatially segregate from genes with CpG-poor promoters by engaging into active (that is, transcription factories) or inactive (that is, polycomb bodies) homotypic chromatin interactions depending on their transcriptional state[50,51]. Therefore, the responsiveness of developmental genes to PEs could depend not only on the presence of PE oCGIs, but also on CGIs located at the target gene promoters. In agreement with this hypothesis, analysis of Hi-C data generated in ESCs[7,52] showed that PEs strongly interact with developmental

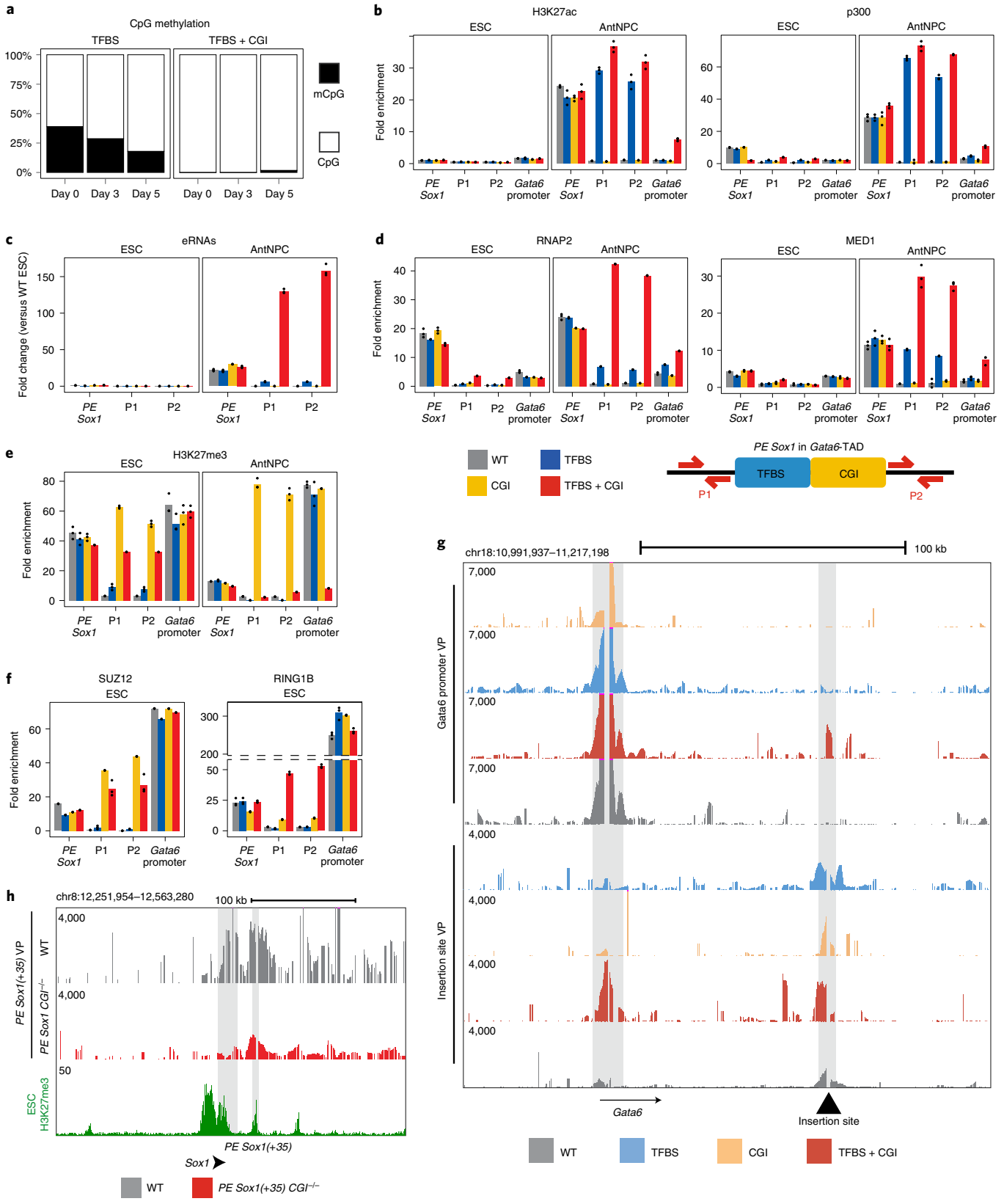

genes with CGI-rich promoters located in the same TADs, but not with genes with CGI-poor promoters (Fig. 4a and Extended Data Fig. 6h). To test whether CpG-poor promoters are responsive to PEs, we inserted the *PE Sox1(+35)* components into the *Gria1*-TAD, approximately 100 kb upstream of the *Gria1*-TSS (Fig. 4b and Extended Data Fig. 7a). Similarly to *Gata6* and *Foxa2*, *Gria1* is not expressed in either ESCs or AntNPCs. However, the *Gria1* promoter does not contain CGIs and is not bound by PcG but fully DNA methylated instead (Fig. 4b). Remarkably, upon differentiation of the *Gria1-TAD* cell lines, none of the *PE Sox1(+35)* inserts were able to induce *Gria1* expression (Fig. 4c and Extended Data Fig. 7b). To gain mechanistic insights into this lack of responsiveness, we measured DNA methylation, H3K27ac, p300, RNAP2, MED1 and eRNA levels around the inserted *PE Sox1(+35)* constructs. Similarly to what we observed within the *Gata6-TAD*, the *TFBS* became demethylated in ESCs, albeit partially, when combined with the *oCGI* (Extended Data Fig. 7c). Furthermore, upon differentiation into AntNPCs, the *TFBS + CGI* and *TFBS* inserts became strongly and similarly enriched in H3K27ac and p300 (Fig. 4d). However, in contrast to what we observed in the *Gata6*-TAD, we did not detect eRNAs around any of the *PE Sox1(+35)* inserts (Fig. 4e). Congruently, the recruitment of RNAP2 and MED1 to the *PE Sox1(+35)* was weak regardless of whether the *TFBS* was alone or with the *oCGI* (Fig. 4f). In addition, RNAP2 and MED1 were not recruited to the *Gria1* promoter, thus in agreement with the lack of *Gria1* induction observed upon differentiation of the *Gria1-TAD* ESC lines (Fig. 4f).

Our results indicate that H3K27ac and eRNA production can be uncoupled from each other and represent different steps during PE activation (Figs. 3b,c and 4d,e). Namely, the accumulation of H3K27ac might occur as PEs become locally activated, while the production of eRNAs, which is coupled with gene transcription, could signify the functional activation of the PEs[39,53]. To assess if these observations could be generalized, we compared eRNA production between three classes of AEs using nascent transcriptomic and epigenomic data generated in ESCs[14,54–56]: (1) Class I enhancers located in TADs containing only poorly expressed genes; (2) Class II enhancers located in TADs with at least one highly expressed gene; and (3) Class III enhancers whose closest gene within the same TAD is highly expressed (Methods). Interestingly, Class I enhancers showed ~2- and 2.5-fold lower eRNA levels than Class II and Class III enhancers, respectively, while H3K27ac levels were similar among the three enhancer groups (Fig. 4g and Extended Data Fig. 7d). These results suggest that enhancer and gene transcription are frequently coupled and mutually dependent on each other[39,57].

**Promoters with large CGI clusters are responsive to PEs.** The experiments within the *Gata6*-TAD suggest that the responsiveness to PEs involves the physical proximity between PEs and their target genes, which in ESCs is likely to be mediated by PcGs present at both PEs and promoters[14,58] (Fig. 3g). ChIP experiments in the *Gria1*-TAD ESC lines revealed that PcGs were recruited to the *PE Sox1(+35)* inserts containing an oCGI (Fig. 5a and Extended Data Fig. 8a), albeit not as strongly as for the *Gata6*-TAD (Fig. 3e,f). Furthermore, the *Gria1* promoter, which does not contain pCGIs, was not bound by PcG (Fig. 5a and Extended Data Fig. 8a). Accordingly, 4C–seq analyses showed that none of the inserted *PE Sox1(+35)* constructs were able to interact with the *Gria1* promoter (Fig. 5b). In principle, the addition of pCGIs to the *Gria1* promoter could increase PcG recruitment and, consequently, the physical and functional communication with the distal *PE Sox1(+35)* constructs. To test this prediction, we introduced one of the *Gata6* pCGIs into the *Gria1* promoter in those ESC lines containing either the *TFBS + CGI* or *TFBS* inserts 100 kb away from the *Gria1*-TSS (Fig. 5c and Extended Data Fig. 8b). Upon differentiation into AntNPCs, the addition of the pCGI did not result in detectable *Gria1* messenger RNA or eRNAs around the *PE* inserts, suggesting that a single CGI is not sufficient to trigger the long-range responsiveness to PEs (Fig. 5c and Extended Data Fig. 8c). Interestingly, in comparison with the PcG levels observed for promoters with large CGI clusters (for example, *Gata6*), the insertion of a single pCGI into the *Gria1* promoter led to relatively mild PcG recruitment (Fig. 5d). This could explain, at least partly, the lack of *Gria1* responsiveness to the distal *PE Sox1(+35)*. Alternatively, the *Gria1* promoter might contain core-promoter elements that are not responsive to developmental enhancers[11,12,59]. To evaluate this possibility, we generated ESC lines in which the *PE Sox1(+35)TFBS* or *PE Sox1(+35) TFBS + CGI* constructs were integrated 380 base pairs (bp) upstream of the *Gria1*-TSS (Fig. 5e and Extended Data Fig. 8d,e). Remarkably, both the *TFBS + CGI* and *TFBS* inserts were able to strongly induce *Gria1* expression upon differentiation into AntNPCs (Fig. 5e and Extended Data Fig. 8f). These results show that the *Gria1* promoter can respond to the *PE Sox1(+35)* and suggest that the boosting effect of the oCGI might be lost when the PEs are located close to gene promoters.

When inserted into the *Gria1*-TAD, the PE *Sox1(+35) TFBS + CGI* did not acquire the same chromatin state as within the *Gata6*-TAD (that is, lower PRC1 levels and higher DNA methylation (Fig. 5a and Extended Data Fig. 7c)). Therefore, the constitutive heterochromatin environment of the *Gria1*-TAD might result in chromatin and/or topological properties at the *PE* insertion site that somehow compromise the regulatory function of the oCGI. To investigate this and further assess whether developmental genes with large CGI clusters in their promoters are particularly responsive to PEs, we inserted the *PE Sox1(+35)* components into the *Sox7/Rp1l1*-TAD, right between *Sox7* and *Rp1l1* (24 kb from *Sox7* and *Rp1l1* TSSs) (Fig. 5f and Extended Data Fig. 8g). *Sox7* and *Rp1l1* are both inactive in ESCs and AntNPCs, but differ in their type of

**Fig. 4 | Genes with CpG-poor promoters do not show long-range responsiveness to PEs. a**, Pile-up plots showing average Hi-C interactions in ESCs[52] between PE-*distal* and developmental genes with CGI-rich promoters ($n = 401$ PE–gene pairs) or genes with CGI-poor promoters ($n = 900$ PE–gene pairs) (Methods). **b**, Strategy to insert the *PE Sox1(+35)* components into the *Gria1*-TAD[80,81]. **c**, *Gria1* and *Sox1* expression was measured by RT–qPCR in ESCs and AntNPCs with the indicated genotypes as in Fig. 2 ($n = 1$ independent biological replicate is shown in Extended Data Fig. 7b). *Gria1* was also measured in the mouse brain to illustrate the quality of the RT–qPCR primers. *Gria1* expression values are presented as arbitrary units (RU) since it was not detectable (ND) except in the brain. For *Sox1*, expression differences between AntNPCs with the *TFBS + CGI* module or the other PE modules were calculated using two-sided nonpaired *t*-tests (NS, not significant; fold-change < 2 or $P > 0.05$). **d**, H3K27ac and p300 levels at the endogenous *PE Sox1(+35)*, the *Gria1*-TAD insertion site (P1 and P2) and the *Gria1* promoter were measured by ChIP–qPCR in cells with the indicated genotypes. ChIP–qPCR signals were calculated as described in Fig. 3. **e**, eRNA levels at the endogenous *PE Sox1(+35)* and the *Gria1*-TAD insertion site (P1 and P2) were measured by RT–qPCR in cells with the indicated genotypes. RT–qPCR signals were calculated as described in Fig. 3. **f**, RNAP2 and MED1 levels were measured by ChIP–qPCR as in **d**. **g**, Violin plots showing H3K27ac and eRNA levels for AEs classified into three categories: Class I (AEs in TADs containing only poorly expressed genes; $n = 271$); Class II (AEs in TADs with at least one highly expressed gene; $n = 2{,}566$); and Class III (AEs whose closest genes in the same TAD are highly expressed; $n = 1{,}294$) (Methods). *P* values were calculated using two-sided unpaired Wilcoxon tests with Bonferroni correction for multiple testing; the numbers in black indicate median fold-changes; the colored numbers correspond to negligible (red) and non-negligible (green) Cliff's delta effect sizes. The violin box graphs were calculated as in Fig. 1.

promoter (Fig. 5f): *Sox7* is an endodermal regulator whose promoter contains a large CGI cluster and is strongly bound by PcG, while *Rp1l1* is specifically expressed in mature rod cells and its promoter does not contain CGIs and is not bound by PcG. Remarkably, upon AntNPC differentiation, none of the *PE Sox1(+35)* inserts were able to induce *Rp1l1* expression (Fig. 5g and Extended Data Fig. 8h). In stark contrast, *Sox7* was strongly induced by the *TFBS + CGI*, while the *TFBS* alone led to a milder gene induction (Fig. 5g and Extended Data Fig. 8h). Together with our experiments in other TADs, these results strongly indicate that developmental genes with large CGI clusters in their promoters are particularly responsive to distal PEs.

**CGIs and TAD boundaries control gene expression specificity.** Our data suggest that, in addition to TAD boundaries, the interactions

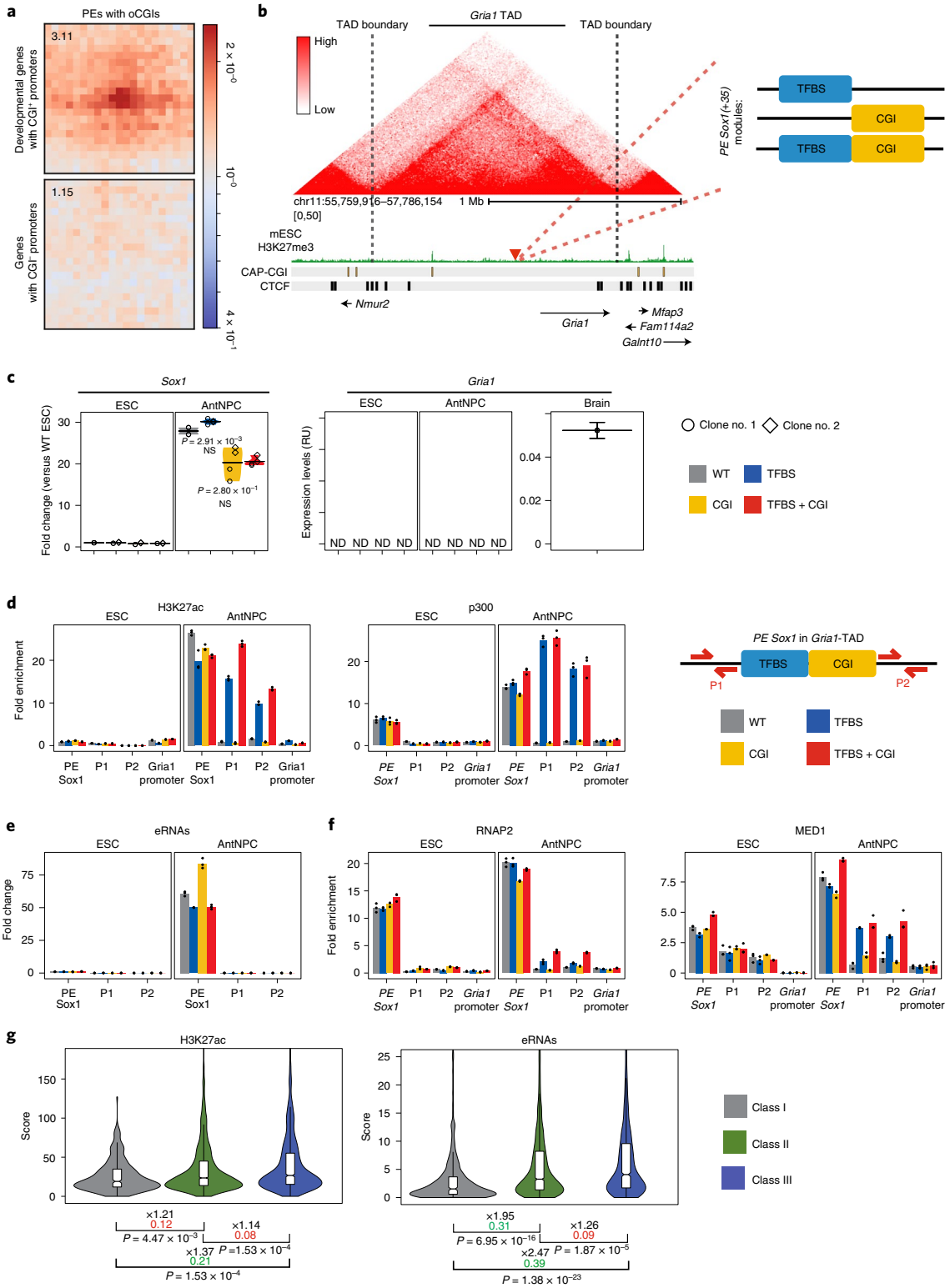

between PE-associated oCGIs and pCGI clusters proximal to developmental genes might contribute to gene expression specificity during embryogenesis. To test this prediction, we genetically engineered two different loci: *Six3/Six2* and *Lmx1a/Lrrc52/Mgst3* (Fig. 6a,d).

We first focused on the *Six3/Six2* locus (Fig. 6a): (1) *Six3* and *Six2* are contained within two neighboring TADs separated by a conserved TAD boundary[60,61]; (2) *Six3* and *Six2* display mutually exclusive expression patterns during embryogenesis (for example,

**Fig. 5 | Promoters with large CGI clusters are particularly responsive to distal PEs. a**, H3K27me3 and RING1B levels at the endogenous *PE Sox1(+35)*, the *Gria1*-TAD insertion site (P1 and P2) and the *Gria1* promoter were measured by ChIP–qPCR in cells with the indicated genotypes. ChIP–qPCR signals were calculated as in Fig. 3. **b**, 4C-seq experiments were performed using the *Gria1*-TAD insertion site as a viewpoint in ESCs with the indicated genotypes. **c**, ESC clonal lines with homozygous insertions of *PE Sox1(+35)TFBS* or *PE Sox1(+35)TFBS + CGI* 100 kb upstream of the *Gria1*-TSS (Fig. 4b), respectively, were used to insert a *Gata6*-pCGI immediately upstream of the *Gria1*-TSS. *Gria1* and *Sox1* expression was measured by RT–qPCR in cells with the indicated genotypes. For the *PE Sox1(+35)TFBS* cells, a single clone was used, while for the *PE Sox1(+35)TFBS + CGI* cells, $n = 2$ independent clonal lines (circles and diamonds) were studied. For each cell line, $n = 2$ replicates of the AntNPC differentiation were performed. The mouse brain expression values are the same as in Fig. 4c. **d**, RING1B and H3K27ac levels at the *Gria1* and *Gata6* promoters were measured by ChIP–qPCR in ESCs with the indicated genotypes. ChIP–qPCR signals were calculated as in Fig. 2. **e**, *Gria1* and *Sox1* expression was measured by RT–qPCR in ESCs and AntNPCs that were WT or homozygous for the indicated *PE Sox1(+35)* modules inserted 380 bp upstream of the *Gria1*-TSS (an independent biological replicate is shown in Extended Data Fig. 8e). For cells with the PE module insertions, two different clonal lines (circles and diamonds) were studied in each case. **f**, Strategy to insert the *PE Sox1(+35)* components into the *Sox7/Rp1l1*-TAD. The red triangle indicates the integration site located in between *Sox7* and *Rp1l1*. **g**, *Sox1*, *Sox7* and *Rp1l1* expression was measured by RT–qPCR in cells with the indicated genotypes. For cells with the PE insertions, $n = 2$ independent clonal lines (circles and diamonds) were studied in each case. In **c**, **e** and **g**, the expression differences between AntNPCs with TFBS + CGI or TFBS were calculated using two-sided nonpaired *t*-tests (***fold-change > 2 and $P < 0.0001$; NS, not significant; fold-change < 2 or $P > 0.05$).

*Six3* in brain; *Six2* in facial mesenchyme)[60]; (3) the *Six3*-TAD contains a PE (that is, *PE Six3(−133)*) that controls the induction of *Six3* in AntNPCs without any effects on *Six2* (ref. [14]); and (4) in ESCs, the *PE Six3(−133)* strongly interacts with *Six3* but not with *Six2* (ref. [14]), although both genes contain multiple pCGIs. Next, we generated ESCs with either a 36-kb deletion spanning the *Six3/Six2*-TAD boundary (*del36*) or a 110-kb inversion that places *Six3* within the *Six2*-TAD and vice versa (*inv110*) (Fig. 6a and Extended Data Fig. 9a,b). Upon differentiation into AntNPCs, *Six2* was strongly induced in *del36* and *inv110* cells (~12- and ~35-fold versus WT, respectively), while *Six3* expression was dramatically reduced in *inv110* cells (~77-fold versus WT) and mildly affected in *del36* cells (~2.5-fold versus WT) (Fig. 6b). In agreement with these gene expression changes, 4C–seq experiments in WT, *del36* and *inv110* ESCs showed that both the boundary deletion and the inversion resulted in increased interactions between *Six2* and *PE Six3(−133)* (Fig. 6c). Furthermore, a CBS immediately upstream of the *PE Six3(−133)* could also contribute to the long-range communication with *Six3/Six2* (Fig. 6a and Extended Data Fig. 9c). However, the deletion of this CBS did not have any major impact on *Six3* or *Six2* expression in either WT or *inv110* AntNPCs, respectively (Extended Data Fig. 9c–e). Altogether, these results indicate that *Six3* and *Six2*, whose promoters have large CGI clusters, are responsive to the *PE Six3(−133)* and, potentially, to other enhancers located within the *Six3*-TAD (ref. [14]).

Next, we focused on the *Lmx1a/Lrrc52/Mgst3* locus (Fig. 6d). *Lmx1a* and *Lrrc52/Mgst3* are located in neighboring TADs separated by a strong TAD boundary. The three genes have different types of promoters[22] and expression patterns in ESCs and AntNPCs[14]. *Lmx1a*, a developmental gene with a large CGI cluster in its promoter, is bound by PcG in ESCs and induced in AntNPCs. *Lrrc52*, a tissue-specific gene without CGIs, is not bound by PcG in ESCs and is inactive in ESCs and AntNPCs. *Mgst3*, a ubiquitously expressed gene with a single and short CGI centered on its TSS, is not bound by PcG and is active in both ESCs and AntNPCs. The *Lmx1a*-TAD contains a PE (that is, *PE Lmx1a(+113)*) that becomes active in AntNPCs and that presumably contributes to *Lmx1a* induction in these cells. Considering all this, we generated two ESC lines with a 260-kb inversion that places *Lmx1a* and *PE Lmx1a(+113)* within the *Lrrc52/Mgst3*-TAD (*inv260*) (Fig. 6d and Extended Data Fig. 9f). Notably, neither *Lrrc52* nor *Mgst3* was induced upon differentiation of the *inv260* ESCs into AntNPCs (Fig. 6e). These results indicate that tissue-specific and housekeeping genes without large CGI clusters in their promoters are not responsive to distal PEs.

Overall, our data suggest that PEs specifically execute their regulatory functions due to the combined effects of TAD boundaries, which provide insulation, and homotypic interactions between oCGIs and pCGIs, which confer enhancer responsiveness (Fig. 7).

## Discussion

Deciphering the factors that control enhancer–promoter compatibility is a major challenge in the enhancer field[62]. According to current models, insulator proteins demarcate TAD boundaries and restrict enhancers to act upon genes located within their same TADs[13,63,64]. Nonetheless, enhancers do not promiscuously activate all the genes present within a TAD[5,8,10,63,65], suggesting that additional factors control enhancer responsiveness. Massively parallel reporter assays in *Drosophila* showed that enhancer responsiveness is determined by the sequence composition of core promoters[12,66]. We now show that, in the context of PE loci, such responsiveness is also dependent on distal genetic elements, namely oCGIs, which serve as tethering elements that allow PEs to preferentially activate promoters containing large CGI clusters (Fig. 7). Although CGIs are considered a vertebrate-specific genomic feature, regulatory sequences with similar tethering functions have been also described in invertebrates[67–69].

Our data suggest that the role of oCGIs as potentiators of PE regulatory functions does not involve the local activation of PEs

**Fig. 6 | oCGIs and TAD boundaries enable PEs to specifically induce their target genes. a**, The TADs in which *Six3* and *Six2* are located (that is, *Six3*-TAD and *Six2*-TAD) are shown according to publicly available Hi-C data[80,81]. Below the Hi-C data, several epigenomic and genetic features of the *Six3*-TAD and the *Six2*-TAD are shown. The dotted rectangles indicate the location of the 36-kb deletion (red) and 110-kb inversion (blue) engineered in ESCs. **b**, The expression of *Six3* (blue) and *Six2* (red) was measured by RT–qPCR in ESCs and AntNPCs that were WT, homozygous for the 36-kb deletion (*del36*) or homozygous for the 110-kb inversion (*inv110*). For each of the engineered structural variants, $n = 2$ clonal cell lines were generated and independently differentiated into AntNPCs. Expression values were calculated as described in Fig. 2. **c**, 4C-seq experiments were performed using the *PE Six3(−133)* as viewpoint in ESCs with the indicated genotypes. **d**, The TADs in which *Lmx1a*, *Lrrc52* and *Mgst3* are located are shown according to publicly available Hi-C data[80,81]. Below the Hi-C data, several epigenomic and genetic features of the corresponding TADs are shown. The dotted rectangle indicates the location of the 260-kb inversion (*inv260*) engineered in ESCs. **e**, The expression of *Lmx1a*, *Mgst3*, *Lrrc52* and *Aldh9a1* was measured by RT–qPCR in cells with the indicated genotypes. For the *inv260*, $n = 3$ clonal cell lines were generated and independently differentiated into AntNPCs. Expression values were calculated as in Fig. 2.

but rather the establishment of long-range interactions with developmental genes (Fig. 7). In pluripotent cells, these PE–gene interactions are likely to be mediated by PRC1 complexes recruited to both oCGIs and pCGIs[14,24,46,70,71]. Intriguingly, our data suggest that the binding of PRC1 to the PEs is increased by the combination of TFBS and oCGIs. While the importance of CGIs as PcG recruitment

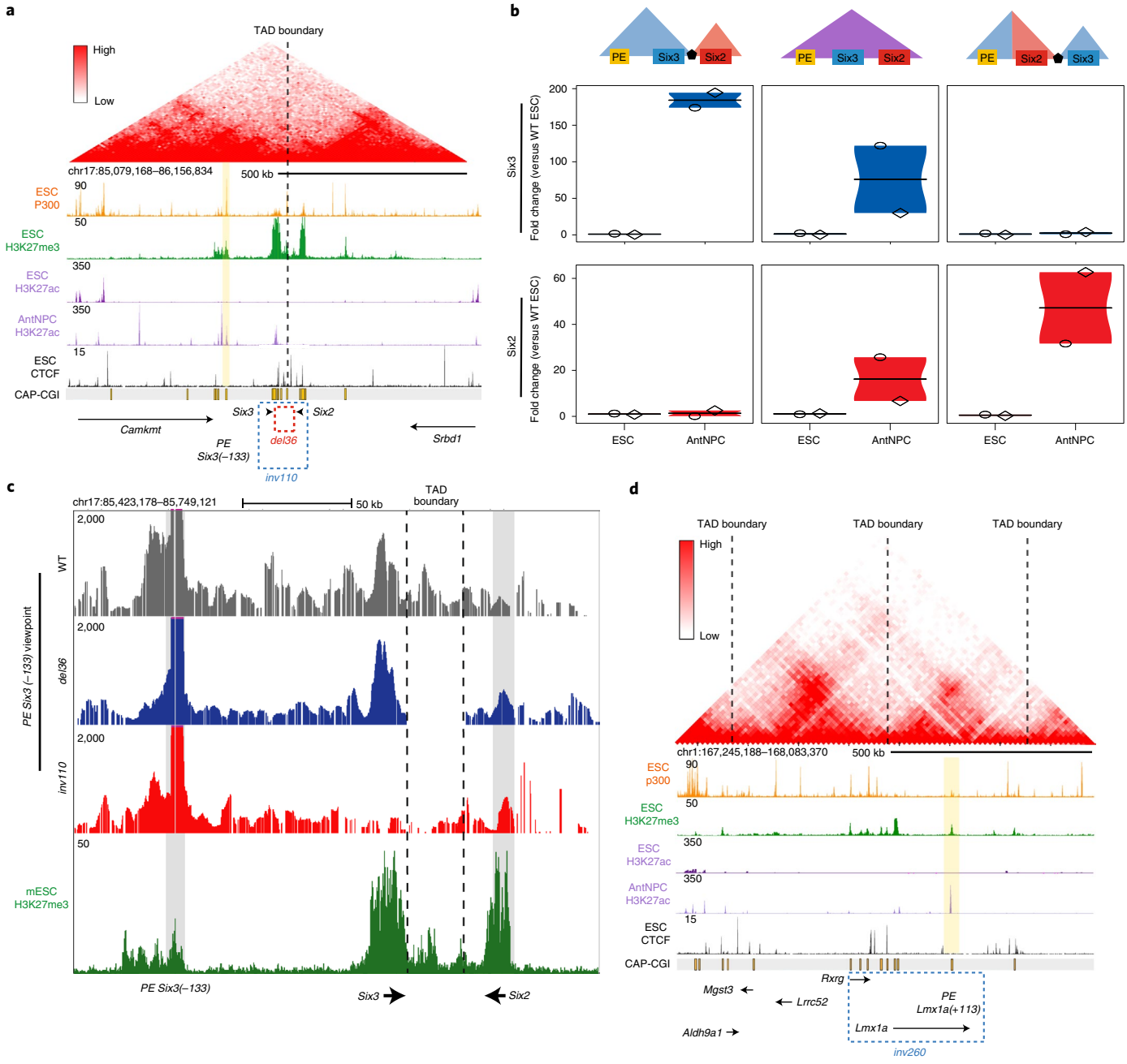

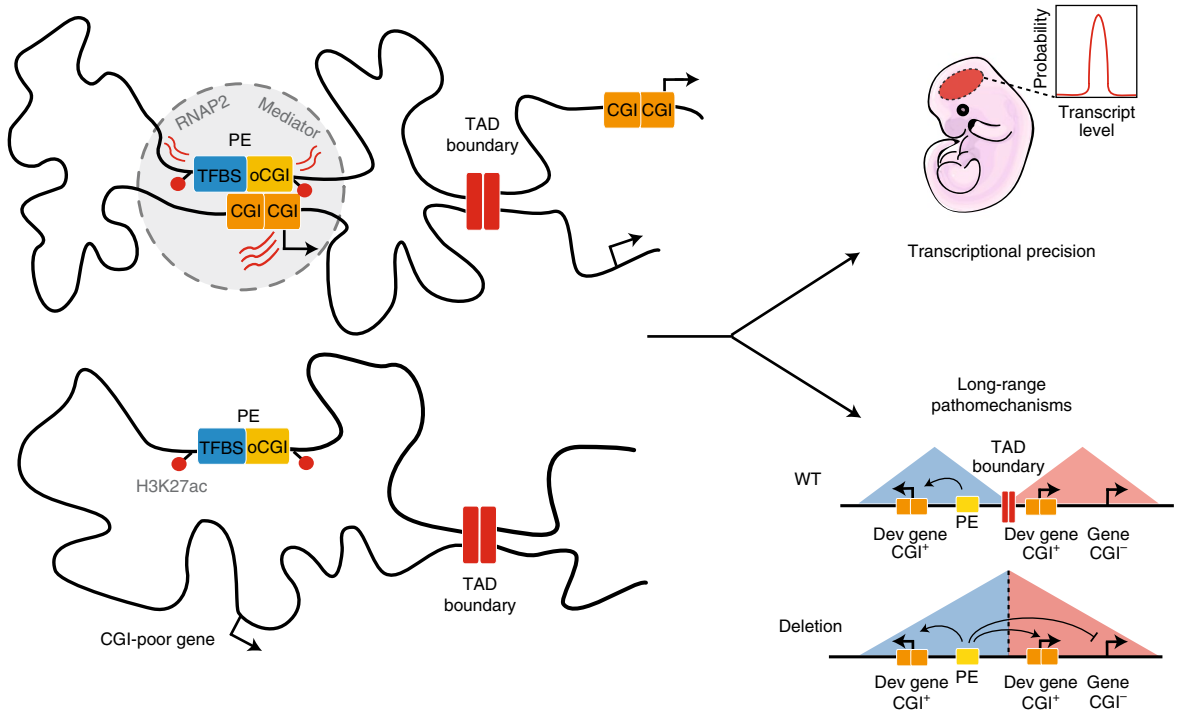


**Fig. 7 | Proposed model for the role of oCGIs as amplifiers of PE regulatory activity and determinants of PE–gene compatibility.** The presence of oCGIs increases the physical communication of PEs with their target genes due to homotypic chromatin interactions between oCGIs and promoter-proximal CGI clusters. Consequently, the oCGIs can increase the number of cells and alleles in which the PEs and their target genes are in close spatial proximity (that is, permissive regulatory topology) both during pluripotency and upon differentiation. This will ultimately result in a timely and homogenous induction of PE target genes once the PEs become active (that is, increase transcriptional precision). In addition, the compatibility and responsiveness between PEs and their target genes depends on the presence of oCGIs at the PEs and of the pCGI clusters at the target genes. Therefore, the oCGIs can increase the specificity of PEs by enabling them to preferentially communicate with their CpG-rich target genes while still being insulated by TAD boundaries. These PE–gene compatibility rules may improve our ability to predict and understand the pathomechanisms of human structural variants.

platforms is well established[24,71], how the TFBS can contribute to PRC1 recruitment is still an open question. Furthermore, our experiments in the *Gria1*-TAD suggest that a single pCGI is not sufficient to enable the long-range communication with PEs. This could be explained, at least partly, by the low levels of PRC1 recruitment that a single CGI can confer in comparison with the large CGI clusters associated with developmental gene promoters. Genetic engineering experiments whereby multiple and long CGIs are inserted in CpG-poor promoters will be required to assess if these genetic features are sufficient to increase the long-range responsiveness to PEs. Regardless, once recruited, PcG complexes might keep PEs and their target genes close together during pluripotent cell differentiation, ensuring that PEs uniformly induce their target genes as they become active. Then, once RNAs are produced at both PEs and their target genes, this would result in PcG eviction[72]. Although PRC1 might also contribute to PE–gene communication once PEs become active[47], additional proteins are likely to be involved in the maintenance of such contacts[73]. Interestingly, upon PE activation the oCGIs increase the loading of Mediator and RNAP2 to both PEs and their target genes (Fig. 3d), suggesting that oCGIs might favor the formation of phase-separated transcriptional condensates[74]. Once PEs are active, multivalent interactions occurring within these condensates could robustly maintain PE–gene communication[74]. According to our analyses, the regulatory function of the PE-associated oCGIs could be primarily attributed to their CpG-richness. Namely, oCGIs can serve as recruitment platforms for ZF-CXXC proteins that, as part of major complexes (for example, PcG, TrxG, Mediator), can facilitate the physical and functional communication between PEs and their target genes[24,75,76]. In addition, TFs with CG-rich binding sites (for example, Sp1)[77,78] might be also recruited to oCGIs and thereby contribute to PE–gene communication. Lastly, some oCGIs might contain binding sites for tissue-specific TFs that are important for the regulatory activity of PEs[79].

We propose a model whereby the precise and specific induction of certain developmental genes is achieved through the combination of CGI-mediated long-range chromatin interactions and the insulation provided by TAD boundaries (Fig. 7). As illustrated by the *TFAP2A* and *EPHA4* loci, the function of CGIs as determinants of enhancer–gene compatibility can help in understanding why only some structural variants that disrupt TAD organization lead to enhancer adoption and major changes in gene expression (Extended Data Fig. 10)[5,9,63]. Therefore, our findings may have important medical implications, as they could improve our ability to predict the pathological consequences of human structural variation[13] (Fig. 7 and Extended Data Fig. 10).

## Online content

Any methods, additional references, Nature Research reporting summaries, source data, extended data, supplementary information, acknowledgements, peer review information; details of author contributions and competing interests; and statements of data and code availability are available at https://doi.org/10.1038/s41588-021-00888-x.

Received: 5 August 2020; Accepted: 17 May 2021;
Published online: 28 June 2021

## References


1. Spitz, F. & Furlong, E. E. M. Transcription factors: from enhancer binding to developmental control. *Nat. Rev. Genet.* **13**, 613–626 (2012).
2. Kvon, E. Z. Using transgenic reporter assays to functionally characterize enhancers in animals. *Genomics* **106**, 185–192 (2015).
3. Furlong, E. E. M. & Levine, M. Developmental enhancers and chromosome topology. *Science* **361**, 1341–1345 (2018).
4. Dixon, J. R. et al. Topological domains in mammalian genomes identified by analysis of chromatin interactions. *Nature* **485**, 376–380 (2012).
5. Laugsch, M. et al. Modeling the pathological long-range regulatory effects of human structural variation with patient-specific hiPSCs. *Cell Stem Cell* **24**, 736–752.e12 (2019).
6. Rao, S. S. P. et al. Cohesin loss eliminates all loop domains. *Cell* **171**, 305–320.e24 (2017).
7. Nora, P. et al. Targeted degradation of CTCF decouples local insulation of chromosome domains from genomic compartmentalization. *Cell* **169**, 930–944 (2017).
8. Ghavi-Helm, Y. et al. Highly rearranged chromosomes reveal uncoupling between genome topology and gene expression. *Nat. Genet.* **51**, 1272–1282 (2019).
9. Kraft, K. et al. Serial genomic inversions induce tissue-specific architectural stripes, gene misexpression and congenital malformations. *Nat. Cell Biol.* **21**, 305–310 (2019).
10. Kikuta, H. et al. Genomic regulatory blocks encompass multiple neighboring genes and maintain conserved synteny in vertebrates. *Genome Res.* **17**, 545–555 (2007).
11. Arnold, C. D. et al. Genome-wide assessment of sequence-intrinsic enhancer responsiveness at single-base-pair resolution. *Nat. Biotechnol.* **35**, 136–144 (2016).
12. Haberle, V. et al. Transcriptional cofactors display specificity for distinct types of core promoters. *Nature* **570**, 122–126 (2019).
13. Spielmann, M., Lupiáñez, D. G. & Mundlos, S. Structural variation in the 3D genome. *Nat. Rev. Genet.* **19**, 453–467 (2018).
14. Cruz-Molina, S. et al. PRC2 facilitates the regulatory topology required for poised enhancer function during pluripotent stem cell differentiation. *Cell Stem Cell* **20**, 689–705.e9 (2017).
15. Rada-Iglesias, A. et al. A unique chromatin signature uncovers early developmental enhancers in humans. *Nature* **470**, 279–283 (2011).
16. Deaton, A. M. & Bird, A. CpG islands and the regulation of transcription. *Genes Dev.* **25**, 1010–1022 (2011).
17. Bell, J. S. K. & Vertino, P. M. Orphan CpG islands define a novel class of highly active enhancers. *Epigenetics* **12**, 449–464 (2017).
18. Illingworth, R. S. et al. Orphan CpG islands identify numerous conserved promoters in the mammalian genome. *PLoS Genet.* **6**, e1001134 (2010).
19. Steinhaus, R., Gonzalez, T., Seelow, D. & Robinson, P. N. Pervasive and CpG-dependent promoter-like characteristics of transcribed enhancers. *Nucleic Acids Res.* **48**, 5306–5317 (2020).
20. Bogdanović, O. et al. Active DNA demethylation at enhancers during the vertebrate phylotypic period. *Nat. Genet.* **48**, 417–426 (2016).
21. Long, H. K. et al. Epigenetic conservation at gene regulatory elements revealed by non-methylated DNA profiling in seven vertebrates. *eLife* **2**, e00348 (2013).
22. Lenhard, B., Sandelin, A. & Carninci, P. Metazoan promoters: emerging characteristics and insights into transcriptional regulation. *Nat. Rev. Genet.* **13**, 233–245 (2012).
23. Williams, K. et al. TET1 and hydroxymethylcytosine in transcription and DNA methylation fidelity. *Nature* **473**, 343–349 (2011).
24. Blackledge, N. P. et al. Variant PRC1 complex-dependent H2A ubiquitylation drives PRC2 recruitment and polycomb domain formation. *Cell* **157**, 1445–1459 (2014).
25. Aljazi, M. B., Gao, Y., Wu, Y., Mias, G. I. & He, J. Cell signaling coordinates global PRC2 recruitment and developmental gene expression in murine embryonic stem cells. *iScience* **23**, 101646 (2020).
26. Habibi, E. et al. Whole-genome bisulfite sequencing of two distinct interconvertible DNA methylomes of mouse embryonic stem cells. *Cell Stem Cell* **13**, 360–369 (2013).
27. Zylicz,J. J. et al. Chromatin dynamics and the role of G9a in gene regulation and enhancer silencing during early mouse development. *eLife* **4**, e09571 (2015).
28. Lee, S. M. et al. Intragenic CpG islands play important roles in bivalent chromatin assembly of developmental genes. *Proc. Natl Acad. Sci. USA* **114**, E1885–E1894 (2017).
29. Bolt, C. C. & Duboule, D. The regulatory landscapes of developmental genes. *Development* **147**, dev171736 (2020).
30. Blackledge, N. P. & Klose, R. CpG island chromatin. *Epigenetics* **2294**, 147–152 (2011).
31. Turberfield, A. H. et al. KDM2 proteins constrain transcription from CpG island gene promoters independently of their histone demethylase activity. *Nucleic Acids Res.* **47**, 9005–9023 (2019).
32. Arab, K. et al. GADD45A binds R-loops and recruits TET1 to CpG island promoters. *Nat. Genet.* **51**, 217–223 (2019).
33. Diez, R. & Storey, K. G. Markers in vertebrate neurogenesis. *Nat. Rev. Neurosci.* **2**, 835–839 (2001).
34. Bentovim, L., Harden, T. T. & DePace, A. H. Transcriptional precision and accuracy in development: from measurements to models and mechanisms. *Development* **144**, 3855–3866 (2017).
35. Boyes, J. & Bird, A. DNA methylation inhibits transcription indirectly via a methyl-CpG binding protein. *Cell* **64**, 1123–1134 (1991).
36. Klemm, S. L., Shipony, Z. & Greenleaf, W. J. Chromatin accessibility and the regulatory epigenome. *Nat. Rev. Genet.* **20**, 207–220 (2019).
37. You, J. S. et al. OCT4 establishes and maintains nucleosome-depleted regions that provide additional layers of epigenetic regulation of its target genes. *Proc. Natl Acad. Sci. USA* **108**, 14497–14502 (2011).
38. Stadler, M. B. et al. DNA-binding factors shape the mouse methylome at distal regulatory regions. *Nature* **480**, 490–495 (2011).
39. Kim, T.-K. et al. Widespread transcription at neuronal activity-regulated enhancers. *Nature* **465**, 182–187 (2010).
40. Mas, G. & Di Croce, L. The role of Polycomb in stem cell genome architecture. *Curr. Opin. Cell Biol.* **43**, 87–95 (2016).
41. Yan, J. et al. Histone H3 lysine 4 monomethylation modulates long-range chromatin interactions at enhancers. *Cell Res.* **28**, 204–220 (2018).
42. Denholtz, M. et al. Long-range chromatin contacts in embryonic stem cells reveal a role for pluripotency factors and polycomb proteins in genome organization. *Cell Stem Cell* **13**, 602–616 (2013).
43. Wang, J. et al. A protein interaction network for pluripotency of embryonic stem cells. *Nature* **444**, 364–368 (2006).
44. Pachano, T., Crispatzu, G. & Rada-Iglesias, A. Polycomb proteins as organizers of 3D genome architecture in embryonic stem cells. *Brief. Funct. Genomics* **18**, 358–366 (2019).
45. Bantignies, F. et al. Polycomb-dependent regulatory contacts between distant Hox loci in *Drosophila*. *Cell* **144**, 214–226 (2011).
46. Isono, K. et al. SAM domain polymerization links subnuclear clustering of PRC1 to gene silencing. *Dev. Cell* **26**, 565–577 (2013).
47. Loubiere, V., Papadopoulos, G. L., Szabo, Q., Martinez, A. M. & Cavalli, G. Widespread activation of developmental gene expression characterized by PRC1-dependent chromatin looping. *Sci. Adv.* **6**, eaax4001 (2020).
48. Benabdallah, N. S. et al. Decreased enhancer-promoter proximity accompanying enhancer activation. *Mol. Cell* **76**, 473–484 (2019).
49. Lim, B., Heist, T., Levine, M. & Fukaya, T. Visualization of transvection in living *Drosophila* embryos. *Mol. Cell* **70**, 287–296.e6 (2018).
50. Beck, S. et al. Implications of CpG islands on chromosomal architectures and modes of global gene regulation. *Nucleic Acids Res.* **46**, 4382–4391 (2018).
51. Liu, S. et al. From 1D sequence to 3D chromatin dynamics and cellular functions: a phase separation perspective. *Nucleic Acids Res.* **46**, 9367–9383 (2018).
52. Kurup, J. T., Han, Z., Jin, W. & Kidder, B. L. H4K20me3 methyltransferase SUV420H2 shapes the chromatin landscape of pluripotent embryonic stem cells. *Development* **147**, dev188516 (2020).
53. Andersson, R., Sandelin, A. & Danko, C. G. A unified architecture of transcriptional regulatory elements. *Trends Genet.* **31**, 426–433 (2015).
54. Lloret-Llinares, M. et al. The RNA exosome contributes to gene expression regulation during stem cell differentiation. *Nucleic Acids Res.* **46**, 11502–11513 (2018).
55. Local, A. et al. Identification of H3K4me1-associated proteins at mammalian enhancers. *Nat. Genet.* **50**, 73–82 (2018).
56. Etchegaray, J. P. et al. The histone deacetylase SIRT6 restrains transcription elongation via promoter-proximal pausing. *Mol. Cell* **75**, 683–699 (2019).
57. Hirabayashi, S. et al. NET-CAGE characterizes the dynamics and topology of human transcribed *cis*-regulatory elements. *Nat. Genet.* **51**, 1369–1379 (2019).
58. Schoenfelder, S. et al. Polycomb repressive complex PRC1 spatially constrains the mouse embryonic stem cell genome. *Nat. Genet.* **47**, 1179–1186 (2015).
59. Butler, J. E. F. & Kadonaga, J. T. Enhancer–promoter specificity mediated by DPE or TATA core promoter motifs. *Genes Dev.* **15**, 2515–2519 (2001).
60. Gómez-Marín, C. et al. Evolutionary comparison reveals that diverging CTCF sites are signatures of ancestral topological associating domains borders. *Proc. Natl Acad. Sci. USA* **112**, 7542–7547 (2015).
61. O'Brien, L. L. et al. Transcriptional regulatory control of mammalian nephron progenitors revealed by multi-factor cistromic analysis and genetic studies. *PLoS Genet.* **14**, e1007181 (2018).
62. Catarino, R. R. & Stark, A. Assessing sufficiency and necessity of enhancer activities for gene expression and the mechanisms of transcription activation. *Genes Dev.* **32**, 202–223 (2018).
63. Lupiáñez, D. G. et al. Disruptions of topological chromatin domains cause pathogenic rewiring of gene-enhancer interactions. *Cell* **161**, 1012–1025 (2015).

64. Kragesteen, B. K. et al. Dynamic 3D chromatin architecture contributes to enhancer specificity and limb morphogenesis. *Nat. Genet.* **50**, 1463–1473 (2018).
65. Li, X. & Noll, M. Compatibility between enhancers and promoters determines the transcriptional specificity of gooseberry and gooseberry neuro in the *Drosophila* embryo. *EMBO J.* **13**, 400–406 (1994).
66. Zabidi, M. A. et al. Enhancer-core-promoter specificity separates developmental and housekeeping gene regulation. *Nature* **518**, 556–559 (2015).
67. Mahmoudi, T., Katsani, K. R. & Verrijzer, C. P. GAGA can mediate enhancer function in *trans* by linking two separate DNA molecules. *EMBO J.* **21**, 1775–1781 (2002).
68. Calhoun, V. C. & Levine, M. Long-range enhancer-promoter interactions in the Scr-Antp interval of the *Drosophila* Antennapedia complex. *Proc. Natl Acad. Sci. USA* **100**, 9878–9883 (2003).
69. Calhoun, V. C., Stathopoulos, A. & Levine, M. Promoter-proximal tethering elements regulate enhancer-promoter specificity in the *Drosophila* Antennapedia complex. *Proc. Natl Acad. Sci. USA* **99**, 9243–9247 (2002).
70. Boyle, S. et al. A central role for canonical PRC1 in shaping the 3D nuclear landscape. *Genes Dev.* **34**, 931–949 (2020).
71. Perino, M. et al. MTF2 recruits Polycomb Repressive Complex 2 by helical-shape-selective DNA binding. *Nat. Genet.* **50**, 1002–1010 (2018).
72. Beltran, M. et al. The interaction of PRC2 with RNA or chromatin is mutually antagonistic. *Genome Res.* **26**, 896–907 (2016).
73. Crispatzu, G. et al. The chromatin, topological and regulatory properties of pluripotency-associated poised enhancers are conserved in vivo. Preprint at *bioRxiv* https://doi.org/10.1101/2021.01.18.427085 (2021).
74. Shrinivas, K. et al. Enhancer features that drive formation of transcriptional condensates. *Mol. Cell* **75**, 549–561.e7 (2019).
75. Dimitrova, E. et al. FBXl19 recruits CDK-Mediator to CpG islands of developmental genes priming them for activation during lineage commitment. *eLife* **7**, e37084 (2018).
76. Long, H. K., Blackledge, N. P. & Klose, R. J. ZF-CxxC domain-containing proteins, CpG islands and the chromatin connection. *Biochem. Soc. Trans.* **41**, 727–740 (2013).
77. Mastrangelo, I. A., Courey, A. J., Wall, J. S., Jackson, S. P. & Hough, P. V. C. DNA looping and Sp1 multimer links: a mechanism for transcriptional synergism and enhancement. *Proc. Natl Acad. Sci. USA* **88**, 5670–5674 (1991).
78. Su, W., Jackson, S., Tjian, R. & Echols, H. DNA looping between sites for transcriptional activation: self-association of DNA-bound Sp1. *Genes Dev.* **5**, 820–826 (1991).
79. Hartl, D. et al. CG dinucleotides enhance promoter activity independent of DNA methylation. *Genome Res.* **29**, 554–563 (2019).
80. Wang, Y. et al. The 3D Genome Browser: a web-based browser for visualizing 3D genome organization and long-range chromatin interactions. *Genome Biol.* **19**, 151 (2018).
81. Bonev, B. et al. Multiscale 3D genome rewiring during mouse neural development. *Cell* **171**, 557–572.e24 (2017).
82. Heinz, S. et al. Simple combinations of lineage-determining transcription factors prime cis-regulatory elements required for macrophage and B cell identities. *Mol. Cell* **38**, 576–589 (2010).
83. Liu, T. et al. Cistrome: an integrative platform for transcriptional regulation studies. *Genome Biol.* **12**, R83 (2011).

## Methods

**Cell lines and differentiation protocol.** E14Tg2a (E14) mouse ESCs were cultured on gelatin-coated plates using Knock-out DMEM (Life Technologies, 10829018) supplemented with 15% FBS (Life Technologies, 10082147) and leukemia inhibitory factor (LIF). For the AntNPC differentiation[84], ESCs were plated at 12,000 cells per $cm^2$ on gelatin-coated plates and grown for 3 d in N2B27 medium supplemented with 10 ng $ml^{-1}$ bFGF (Life Technologies, PHG0368) without serum or LIF. Subsequently, cells were grown for another 2 d in N2B27 medium without bFGF (days 3–5). From day 2 to day 5, the N2B27 medium was supplemented with 5 mM Xav939 (ref. [85]) (Sigma, 284028-89-3). N2B27 medium: Advanced DMEM F12 (Life Technologies, 21041025) and Neurobasal medium (Life Technologies, 12348017) (1:1), supplemented with 1× N2 (Life Technologies, 17502048), 1× B27 (Life Technologies, 12587010), 2 mM L-glutamine (Life Technologies, 25030024), 40 mg $ml^{-1}$ BSA (Life Technologies, 15260037) and 0.1 mM 2-mercaptoethanol (Life Technologies, 31350010).

**RNA isolation, complementary DNA synthesis and quantitative PCR with reverse transcription.** Total RNA was isolated using Innuprep RNA Mini Kit (Analytik Jena, 845-KS-2040250). cDNA was generated using ProtoScript II First Strand cDNA Synthesis Kit (New England Biolabs, E6560L). Quantitative PCR with reverse transcription (RT–qPCR) analyses were performed on the Light Cycler 480II (Roche) using *Eef1a1* and *Hptr* as housekeeping genes. For each sample, RT–qPCRs were performed as technical triplicates using primers listed in Supplementary Data 1.

**ChIP.** First, $5 \times 10^7$ (p300/RNAP2/MED1/PcG ChIPs) or $1 \times 10^7$ (histone ChIPs) cells were crosslinked with 1% formaldehyde for 10 min at room temperature and quenched with 0.125 M glycine for 10 min. Cells were washed and resuspended sequentially in three lysis buffers (Buffer 1: 50 mM HEPES, 140 mM NaCl, 1 mM EDTA, 10% glycerol, 0.5% NP-40, 0.25% Triton X-100; Buffer 2: 10 mM Tris, 200 mM NaCl, 1 mM EDTA, 0.5 mM EGTA; Buffer 3: 10 mM Tris, 100 mM NaCl, 1 mM EDTA, 0.5 mM EGTA, 0.1% Na-deoxycholate, 0.5% *N*-lauroylsarcosine) to isolate chromatin. Chromatin was sonicated for 15 cycles (20 s on, 30 s off, 25% amplitude) using an EpiShear probe sonicator (Active Motif). Sonicated chromatin was incubated overnight at 4 °C with 3 µg of antibody for histones or 10 µg of antibody for other proteins. Next, 50 µl of Protein G magnetic beads (Invitrogen, 10004D) was added and incubated for 4 h at 4 °C. Magnetic beads were washed and the chromatin eluted, followed by de-crosslinking and DNA purification. The ChIP and input DNAs were analyzed by quantitative PCR (qPCR) using two *mm10* intergenic regions as negative controls (chr2:73,030,265-73,030,373; chr6: 52,339,345-52,339,505). The qPCRs for each sample were performed as technical triplicates. All antibodies and primers used in ChIP–qPCR experiments are listed in Supplementary Data 1.

**Bisulfite sequencing.** Bisulfite conversion of 400 ng of genomic DNA was performed using the EZ DNA Methylation Kit (Zymo Research, D5001). The investigated sequences were amplified by PCR using EpiTaq polymerase (Takara Bio, R110B) and primers described in Supplementary Data 1. PCR products were cloned into the pGEM-T vector (Promega, A1360) and sequenced with the M13 reverse primer.

**Immunofluorescence.** Cells were fixed for 10 min in 3.7% paraformaldehyde at room temperature, permeabilized with 0.1% Triton X-100 for 15 min at room temperature and blocked in PBS with 5% BSA for 1 h at room temperature. Cells were incubated with primary antibodies (anti-GATA6 (AF1700, R&D Systems, 8 µl $ml^{-1}$) or anti-SOX1 (AF3369, R&D Systems, 8 µl $ml^{-1}$)) in blocking solution overnight at 4 °C, rinsed and incubated with secondary antibodies (Fig. 2g: donkey anti-goat IgG Alexa Fluor Plus 488 (A32814, Invitrogen, 1 µl $ml^{-1}$); Extended Data Fig. 5c: donkey anti-goat IgG Alexa Fluor Plus 594 (A32758, Invitrogen, 1 µl $ml^{-1}$)) in blocking solution for 30 min at room temperature. Nuclei were stained with DAPI (Sigma, 28718-90-3) and mounted with anti-fading mounting medium (Life Technologies, P10144).

**4C–seq.** In total, $1 \times 10^7$ cells were crosslinked with 1% formaldehyde for 20 min and quenched with 0.125 M glycine for 10 min. Cells were washed with PBS and resuspended in lysis buffer (50 mM Tris-HCl pH 7.5, 150 mM NaCl, 5 mM EDTA, 0.5% NP-40, 1% Triton X-100 and 1× protease inhibitors) during 10 min on ice. Following centrifugation, nuclei were resuspended in 0.5 ml of 1.2× restriction buffer with 0.3% SDS and incubated at 37 °C/900 r.p.m. for 1 h. Triton X-100 was added to a concentration of 2% followed by 1 h of incubation at 37 °C/900 r.p.m. Next, chromatin was digested overnight at 37 °C/900 r.p.m. with 400 U of NlaIII (R0125L, NEB). NlaIII was inactivated by adding SDS to a concentration of 1.6% and incubating for 20 min at 65 °C/900 r.p.m. The digested chromatin was mixed with 6.125 ml of 1.15× ligation buffer (50 mM Tris-HCl pH 7.6, 10 mM $MgCl_2$, 1 mM ATP, 1 mM dithiothreitol). Triton X-100 was added to a concentration of 1% and the solution was incubated for 1 h at 37 °C while shaking gently. The digested chromatin was ligated with 100 U of T4 DNA ligase (15224-041, Life Technologies) for 8 h at 16 °C, followed by RNase A treatment (Peqlab, 12-RA-03) for 45 min at 37 °C. Subsequently, chromatin was de-crosslinked with 300 mg of Proteinase K (Peqlab, 04-1075) and incubated at 65 °C overnight. DNA was purified by phenol/chloroform extraction and ethanol precipitation, resuspended in 100 ml of water and digested with 50 U of DpnII (R0543M, NEB) at 37 °C overnight. DNA samples were purified by phenol/chloroform extraction and ethanol precipitation and resuspended in 500 µl of $H_2O$. Then, 200 U of T4 DNA Ligase was added into a final volume of 14 ml of 1× Ligation Buffer, followed by overnight incubation at 16 °C. DNA samples were subjected to phenol/chloroform extraction and ethanol precipitation, resuspended in 100 µl of water and column-purified (28104, QIAgen). The resulting DNA products were amplified by inverse PCR using primers located within selected viewpoints (Supplementary Data 1) and the Expand Long Template PCR System (11681842001, Roche) (94 °C 2 min, 30× (94 °C 10 s, 60 °C 1 min, 68 °C 3 min), 68 °C 5 min).

**oCGI deletion using CRISPR–Cas9.** To generate the deletion of the *PE Sox1(+35) CGI*, a pair of single guide RNAs (sgRNAs) flanking the oCGI were designed with Benchling's CRISPR toolkit (www.benchling.com) (Supplementary Data 1). For each sgRNA, two oligonucleotides were synthesized (IDT), annealed and cloned into a CRISPR–Cas9 expression vector (pX330-hCas9-long-chimeric-grna-g 2p; Leo Kurian's laboratory). ESCs were transfected with the pair of gRNAs–Cas9-expressing vectors using Lipofectamine (Thermo Scientific, L3000001). After 16 h, puromycin selection was performed for 48 h. Surviving cells were isolated in 96-well plates by serial dilution and clones with the deletion were identified by PCR using primers listed in Supplementary Data 1. The presence of the deletion was confirmed by Sanger sequencing.

**Homology-dependent knock-in.** Knock-In of PE modules was performed as previously described in ref. [86]. Briefly, an sgRNA was designed for the insertion site of interest and cloned in the CRISPR–Cas9 expression described above. Then, the cassette-vector was generated by ligating: (1) 300-bp homology arms flanking the insertion site; (2) construct of interest; and (3) cloning vector. The resulting cassette-vector was used as a template for amplifying the knock-in donor (left homology arm + construct + right homology arm) by PCR (Supplementary Data 2). The resulting PCR product was column-purified (28104, QIAgen). ESCs were transfected with the sgRNA–Cas9-expressing vector and the knock-in donor using Lipofectamine (Thermo Scientific, L3000001). After 16 h, puromycin selection was performed for 48 h. Surviving cells were isolated in 96-well plates by serial dilution and clones with insertions were identified by PCR using the primers listed in Supplementary Data 1. The PE insertions were confirmed by Sanger sequencing.

**FAIRE.** Chromatin was sonicated as described for ChIP and then subjected to three rounds of phenol/chloroform purification followed by ethanol precipitation[87]. The FAIRE and input DNA was analyzed by qPCR using two *mm10* intergenic regions as negative controls (chr2:73,030,265-73,030,373; chr6:52,339,345-52,339,505) and the primers listed in Supplementary Data 1.

**NOMe-PCR.** Nuclei extraction and M.CviPI treatment were performed as described previously[88]. Briefly, isolated nuclei were incubated with 200 U of M.CviPI (NEB, M0227L) for 15 min at 37 °C. Then, bisulfite conversion was performed using the EZ DNA Methylation Kit (Zymo Research, D5001) and the converted DNA was amplified by PCR. PCR products were cloned into the pGEM-T vector (Promega, A1360) and sequenced with the M13 reverse primer. NOMe-PCR data were analyzed with the NOMePlot web app tool (http://www.landeiralab.ugr.es/software)[88].

**Computational and statistical analyses.** *Statistics and reproducibility.* Immunofluorescence assays and genotyping of all the ESC lines were independently performed twice with similar results.

For RT–qPCR measurements in transgenic cell lines, expression levels were measured in two independent biological replicates. In each of these biological replicate experiments, two different clonal cell lines for each of the investigated genotypes were generally studied (unless stated otherwise), and for each clonal cell line two replicates of the AntNPC differentiation were measured. The statistical significance of the expression differences was calculated between AntNPCs with the TFBS + CGI module and AntNPCs with the other PE modules whenever the number of biological replicates was $n \geq 3$.

*Analyses of qPCR data.* For RT–qPCR, relative gene expression levels were calculated with the comparative delta Ct method ($2^{\Delta Ct}$), whereby the differences in Ct values between the genes of interest and two housekeeping genes (*Eef1a* and *Hprt*) were considered. Primers can be found in Supplementary Data 1.

For ChIP–qPCR, for each sample, signals were calculated as percentage of input using technical triplicates and normalized to the average signals obtained in the same sample for two negative control regions (Chr2_neg and Chr6_neg; Supplementary Data 1).

*aCGI design.* The aCGI was designed by randomly incorporating nucleotides into an 800-bp sequence with a 50% higher chance of incorporating C or G rather than A or T. These GC-rich sequences were filtered to fulfill the Gardiner–Garden criteria (that is, observed/expected ratio of CpGs > 0.6 and G + C percentage

(GC%) > 50%)[89]. Then, the resulting CGIs were analyzed with the EMBOSS Cpgplot[90] and only those sequences with high GC% along the whole sequence were selected as possible candidates for synthesis. Finally, the sequence with lowest complexity was ordered as a gBlock from IDT (Supplementary Data 2).

*4C–seq analysis.* 4C–seq samples were sequenced on an Illumina HiSeq 2500 sequencer, generating single reads of 74 bases in length. Reads were assigned to samples based on their first 10 bases, the primer sequences were removed from the reads and the remaining sequences were trimmed to 36 bases per read. These 36 bases were aligned to the *mm10* reference genome using the HISAT2 aligner[52]. From these alignments, the reads per NlaIII restriction fragment were quantified using bedtools[91]. Then, the reads mapping to the viewpoint as well as the preceding and following restriction fragments were removed. Finally, the resulting bedgraph files were normalized as reads per million, considering the total number of mappable reads left for each sample. These normalized bedgraph files were used for downstream visualization of the 4C–seq data.

*Gene annotation.* The RefSeq gene annotation was downloaded from University of California Santa Cruz (UCSC) Table Browser[92] and used for the different analyses described in this work.

*ChIP–seq and PRO-seq preprocessing steps.* ChIP–seq or precision nuclear run-on sequencing (PRO-seq) fastq files read quality was assessed with FastQC (http://www.bioinformatics.babraham.ac.uk/projects/fastqc/) and *MultiQC*[93].

For ChIP–seq data, the removal of read adapters and low-quality filtering was done with trimmomatic[94].

For PRO-seq data, adapter removal was performed with cutadapt v.1.18 (ref. [95]), filtering for a minimum of 15 bases (adapter sequence: TGGAATTCTCGGGTGCCAAGG). In addition, reads mapping to mouse ribosomal DNA repeats (BK000964.3) were discarded.

For both data types, reads were mapped to the *mm9* reference genome with Bowtie2 (ref. [96]). For ChIP–seq samples duplicated reads were discarded with SAMtools[97].

**Genetic properties of CGIs.** *Data retrieval and preprocessing.* PE coordinates were downloaded from ref. [14]. Only PEs >2.5 kb away from any TSS (*PE-all*) were considered. PEs >10 kb away from any TSS are referred to as *PE-distal*.

NMI coordinates were obtained from ref. [21]. CAP-CGI coordinates were obtained from ref. [18]. Computational CGIs (GC content >50%; length > 200 bp; CpG observed to expected ratio >0.6) were retrieved from the UCSC browser.

H3K27me3 ChIP–seq data generated in ESCs (GSE89209; H3K27me3: SRR4453259, input: SRR4453262) were used to call H3K27me3 peaks using *MACS2* (ref. [98]) with broad peak calling mode. Peaks with a fold-enrichment > 3 and *Q* value < 0.1 were considered. Subsequently, peaks within 1 kb of each other were merged using bedtools, and associated with a protein-coding gene when overlapping a TSS. Lastly, the knee of the size distribution of the H3K27me3 peaks associated with genes was determined with findiplist() (inflection R package; https://cran.r-project.org/web/packages/inflection/vignettes/inflection.html). Upon curvature analysis, genes with an H3K27me3 peak >6 kb were considered as developmental genes (*devTSS*).

NMIs and CAP-CGIs were associated with *PE-distal* or *devTSS* if located <3 kb away from them. In addition, to create a group of random regions, each region associated with a *PE-distal* was randomly relocated along the genome 1,000 times (maintaining its size).

*Sequence composition.* To retrieve DNA sequences, BSgenome[99] and the unmasked *mm9* genome were used. The length, GC%, CpG percentage (CpG%) and CpG observed/expected ratio were calculated for each region. The CpG% was calculated as the ratio of CpG dinucleotide counts with respect to half the total region length. The CpG observed/expected ratio was calculated as described in ref. [89].

*CGI block sizes.* All CAP-CGIs <3 kb from the region of interest (PE or TSS) were obtained, with smaller and larger CGI coordinates constituting the CGI block initial limits. If another CAP-CGI was encountered in the next 5 kb from the CGI block limits, it was added to it, and the CGI block limits were expanded, taking into account the newly included CGI. The second step was recursively applied until no CGI was found in the next 5 kb.

**Comparison of eRNA levels between different classes of AEs.** *Data retrieval and preprocessing.* Gene expression levels measured in fragments per kilobase of transcript per million mapped reads (FPKMs) and AE coordinates from WT ESCs were obtained from ref. [14]. To avoid confounding effects between transcripts produced by enhancers or genes, only active intergenic enhancers located >10 kb from any TSS and >20 kb from any transcription termination site were considered[100].

For the analyses presented in Fig. 4g and Extended Data Fig. 7d (left), the H3K27ac ChIP–seq fastq files were retrieved from GEO (GSM2360929; sample ID: SRR4453258) and preprocessed as indicated above. For the analyses presented in Extended Data Fig. 7d (middle and right), two H3K27ac bigWig files were downloaded from GEO (GSM2808655 and GSM2808669).

For Fig. 4g and Extended Data Fig. 7d (left), PRO-seq fastq files were obtained from GEO (GSE115713; sample IDs: SRR7300121, SRR7300122) and the two replicates were combined and preprocessed as described above. For Extended Data Fig. 7d (middle and right), two PRO-seq bigWig files (one for each DNA strand) were obtained from GEO (GSE130691).

TAD maps from ESCs were retrieved from refs. [80,81]. For Fig. 4g and Extended Data Fig. 7d (left): mESC_Dixon2012-raw_TADs.txt. For Extended Data Fig. 7d (middle and right): mESC.Bonev_2017-raw.domains.

*H3K27ac and PRO-seq enhancer levels quantification.* Figure 4g and Extended Data Fig. 7d (left): H3K27ac and PRO-seq reads with a mapping quality <10 were discarded using SAMtools[97]. Next, bigwig files were generated with deepTools[101] using bamCoverage (reads per genomic content normalization) and then used to calculate the H3K27ac and PRO-seq enhancer mean scores with computeMatrix from deepTools. For H3K27ac and PRO-seq, the signals were calculated using a ±1-kb or ±0.5-kb window from the enhancer midpoints, respectively.

Extended Data Fig. 7d (middle and right): H3K27ac and PRO-seq mean signals for the enhancers were calculated with the bigWigAverageOverBed UCSC binary tool. PRO-seq signals for each enhancer from the two different strands were averaged and the same was done for the signals coming from different H3K27ac replicates.

*AEs classification.* Three groups of AEs were defined: (1) Class I enhancers located in TADs only containing poorly expressed genes (<0.5 FPKM); (2) Class II enhancers located in TADs with at least one gene with >10 FPKM; (3) Class III enhancers whose closest gene within the same TAD has >10 FPKM.

*Balancing of H3K27ac levels within enhancer classes.* Enhancers with similar H3K27ac levels belonging to the three enhancer classes were selected by applying the nearest neighbor matching method (without replacement and ratio = 1) using MatchIt (https://cran.r-project.org/web/packages/MatchIt/MatchIt.pdf) and considering the enhancer group I as the treatment condition.

*Cliff's delta effect size estimator.* Cliff's delta[102,103] was used to quantify the differences between groups of genomic regions. This measure is robust to skewed signal distributions[104]. Cliff's delta was estimated using the cliff.delta() function from the R package effsize (https://cran.r-project.org/web/packages/effsize/index.html). Differences between groups with |delta| < 0.147 can be considered as negligible and |delta| ≥ 0.147 as non-negligible.

**Hi-C analyses.** *Preprocessing.* GSE130723: the .hic files for two Hi-C replicates (GSM3752487, GSM3752488) generated in ESCs were downloaded. The .hic format was converted to .cool format using a 5-kb matrix resolution with the hic2cool software (https://github.com/4dn-dcic/hic2cool).

GSE98671: the .cool format files for two untreated ESC Hi-C replicates (GSM2644945, GSM2644946) at a 20-kb matrix resolution were downloaded.

For both datasets the corresponding replicates in .cool format were merged with cooler merge[105] and normalized with cooler balance[105].

*Definition of PE–gene pairs.* Group A. When a *PE-distal* was found in a TAD with a *devTSS*, both coordinates were selected to define a PE–gene pair. Only *devTSS* with a CAP-CGI in <3 kb were considered.

Group B. CGI-poor TSSs do not have a CAP-CGI in <3 kb and are not enriched in H3K27me3 (H3K27me3 ChIP–seq peaks described above). When a *PE-distal* was found in a TAD with a CGI-poor TSS, both coordinates were selected to define a PE–gene pair.

Two additional filters were applied: (1) PE–gene pairs were balanced to compare groups of PE–gene pairs without significant differences in their linear genomic sizes. PE–gene pairs with similar lengths were selected by applying the nearest neighbor matching method (without replacement and ratio = 1) using MatchIt (https://cran.r-project.org/web/packages/MatchIt/MatchIt.pdf) and considering Group A as the treatment condition; (2) only TSSs of genes with expression <1 FPKM were considered.

We used TADs defined in mESC_Dixon2012-raw_TADs.txt[80].

*Pile-up plot generation.* The pile-up plots for the GSE130723 and GSE98671 Hi-C datasets were generated with coolpup.pyc[106] using a padding of ±50 kb or ±100 kb, respectively.

**TF motif analyses.** The genomic coordinates of PEs and AEs were defined by p300 peaks identified in ESCs[14] and located >2.5 kb away from any RefSeq TSS.

*CAP-CGI versus p300 peaks.* Among the previously reported PEs[14], we considered only those with a CAP-CGI in <3 kb and that did not overlap with the p300 peaks defining the PEs. Then, motif analyses were performed separately for the CAP-CGIs and the p300 peaks associated with the selected PEs using Homer[82] and SeqPos[83].

*Homer.* Input regions (p300 peaks or CAP-CGIs) were analyzed with the following parameters: -size given -mset vertebrates.

*SeqPos.* A curated cistrome motif database and de novo motif searches were used. The species list parameter was used to filter the results considering both *Homo sapiens* and *Mus musculus*. All other parameters were used with the default settings.

*PEs versus AEs.* We considered PEs with a CAP-CGI in <3 kb and AEs without a CAP-CGI in <3 kb. The motif composition of PEs and AEs was analyzed using two different tools:

(i) Homer[82] was utilized to analyze each enhancer group separately with the same parameters described above.
(ii) AME[107] was used to perform a differential motif enrichment analysis between PEs and AEs. The Eukaryote DNA & Vertebrates motif database was used. All other parameters were used with default settings.

**Whole-genome bisulfite sequencing analysis.** For whole-genome bisulfite sequencing analyses we used public data from ESCs cultured with MEK and GSK3 inhibitors (2i)[26], day 2 epiblast-like cells (EpiLCs)[27], epiblast stem cells (EpiSCs)[27], serum + LIF ESCs (GSE82125) and neural progenitor cells (GSE82125). The adapters were trimmed with Trim Galore and mapped to the *mm10* reference genome using Bismark-v.0.16.1 (ref. [108]) and bowtie2 v.2.2.9 (ref. [109]). For each cell type, the CpG methylation levels were estimated with the Bismark methylation extractor, considering only CpGs with a coverage of 3–100 reads. For visualization of CpG methylation levels around pCGIs and oCGIs, the average CpG methylation signal was visualized with deeptools v.3.3.1 (ref. [101]).

**ChIP–seq profile plots.** *PE classification. PE-distal* were separated into four groups: (1) PEs with overlapping TFBS/p300 and CAP-CGIs; (2) PEs with TFBS/p300 separated by 1 bp to 1 kb from a CAP-CGI; (3) PEs with TFBS/p300 separated by 1–3 kb from a CAP-CGI; and (4) PEs without CAP-CGIs in 3 kb. The coordinates of AEs without CAP-CGI in <3 kb were also considered.

*Datasets used.* H3K27me3: GSE157748 (Extended Data Fig. 1b, left) and GSE89209 (Extended Data Fig. 1b, right) H3K27me3 ChIP–seq datasets from ESCs were used. For GSE89209, the fastq file SRR4453259 was processed as described in previous sections. For GSE157748, bigwig files (GSM4774518, GSM4774519) were downloaded and combined using bigWigMerge and bedGraphToBigWig UCSC tools[110].

TET1: GSE104067 was used. The bigwig files of three untreated ESC replicates (GSM2788888, GSM2788889, GSM2788890) were downloaded and combined using bigWigMerge and bedGraphToBigWig UCSC tools[110].

KDM2B: GSE126862 was used. The bigwig file with all the merged untreated ESC replicates (GSE126862_KDM2AB_CXXCfl_KDM2B_UNT_mm10_downsampled_merged.bw) was downloaded. Bigwig coordinates were converted from *mm10* to *mm9* with CrossMap[111].

*Plots generation.* Profiles plots were generated using computeMatrix and plotProfile from deepTools[101].

**Reporting Summary.** Further information on research design is available in the Nature Research Reporting Summary linked to this article.

## Data availability

All the 4C–seq data generated in this study are available through the GEO (GSE156465). All the generated transgenic ESC lines are available upon request.

## References


84. Gouti, M. et al. In vitro generation of neuromesodermal progenitors reveals distinct roles for wnt signalling in the specification of spinal cord and paraxial mesoderm identity. *PLoS Biol.* **12**, e1001937 (2014).
85. Matsuda, K. & Kondoh, H. Dkk1-dependent inhibition of Wnt signaling activates Hesx1 expression through its 5′ enhancer and directs forebrain precursor development. *Genes Cells* **19**, 374–385 (2014).
86. Yao, X. et al. Tild-CRISPR allows for efficient and precise gene knockin in mouse and human cells. *Dev. Cell* **45**, 526–536.e5 (2018).
87. Giresi, P. G., Kim, J., McDaniell, R. M., Iyer, V. R. & Lieb, J. D. FAIRE (Formaldehyde-Assisted Isolation of Regulatory Elements) isolates active regulatory elements from human chromatin. *Genome Res.* **17**, 877–885 (2007).
88. Requena, F. et al. NOMePlot: analysis of DNA methylation and nucleosome occupancy at the single molecule. *Sci. Rep.* **9**, 8140 (2019).
89. Gardiner-Garden, M. & Frommer, M. CpG islands in vertebrate genomes. *J. Mol. Biol.* **196**, 261–282 (1987).
90. Madeira, F. et al. The EMBL-EBI search and sequence analysis tools APIs in 2019. *Nucleic Acids Res.* **47**, W636–W641 (2019).
91. Quinlan, A. R. & Hall, I. M. BEDTools: a flexible suite of utilities for comparing genomic features. *Bioinformatics* **26**, 841–842 (2010).
92. Karolchik, D. et al. The UCSC Table Browser data retrieval tool. *Nucleic Acids Res.* **32**, 493–496 (2004).
93. Ewels, P., Magnusson, M., Lundin, S. & Käller, M. MultiQC: summarize analysis results for multiple tools and samples in a single report. *Bioinformatics* **32**, 3047–3048 (2016).
94. Bolger, A. M., Lohse, M. & Usadel, B. Trimmomatic: a flexible trimmer for Illumina sequence data. *Bioinformatics* **30**, 2114–2120 (2014).
95. Martin, M. Cutadapt removes adapter sequences from high-throughput sequencing reads. *EMBnet J.* **17**, 10–12 (2011).
96. Langmead, B. & Salzberg, S. L. Fast gapped-read alignment with Bowtie 2. *Nat. Methods* **9**, 357–359 (2012).
97. Li, H. et al. The Sequence Alignment/Map format and SAMtools. *Bioinformatics* **25**, 2078–2079 (2009).
98. Feng, J., Liu, T., Qin, B., Zhang, Y. & Liu, X. S. Identifying ChIP-seq enrichment using MACS. *Nat. Protoc.* **7**, 1728–1740 (2012).
99. Pagès, H. BSgenome: software infrastructure for efficient representation of full genomes and their SNPs. R package version 1.56.0 (2020).
100. Wang, J. et al. Nascent RNA sequencing analysis provides insights into enhancer-mediated gene regulation. *BMC Genomics* **19**, 633 (2018).
101. Ramírez, F. et al. deepTools2: a next generation web server for deep-sequencing data analysis. *Nucleic Acids Res.* **44**, W160–W165 (2016).
102. Cliff, N. Dominance statistics: ordinal analyses to answer ordinal questions. *Psychol. Bull.* **114**, 494–509 (1993).
103. Macbeth, G., Razumiejczyk, E. & Ledesma, R. D. Cliff´s Delta Calculator: a non-parametric effect size program for two groups of observations. *Univ. Psychol.* **10**, 545–555 (2011).
104. Bush, S. J., McCulloch, M. E. B., Summers, K. M., Hume, D. A. & Clark, E. L. Integration of quantitated expression estimates from polyA-selected and rRNA-depleted RNA-seq libraries. *BMC Bioinformatics* **18**, 301 (2017).
105. Abdennur, N. & Mirny, L. A. Cooler: scalable storage for Hi-C data and other genomically labeled arrays. *Bioinformatics* **36**, 311–316 (2020).
106. Flyamer, I. M., Illingworth, R. S. & Bickmore, W. A. Coolpup.py: versatile pile-up analysis of Hi-C data. *Bioinformatics* **36**, 2980–2985 (2020).
107. Bailey, T. L. et al. MEME Suite: tools for motif discovery and searching. *Nucleic Acids Res.* **37**, 202–208 (2009).
108. Krueger, F. & Andrews, S. R. Bismark: a flexible aligner and methylation caller for bisulfite-seq applications. *Bioinformatics* **27**, 1571–1572 (2011).
109. Langmead, B. & Salzberg, S. L. Fast gapped-read alignment with Bowtie 2. *Nat. Methods* **9**, 357–359 (2012).
110. Kent, W. J., Zweig, A. S., Barber, G., Hinrichs, A. S. & Karolchik, D. BigWig and BigBed: enabling browsing of large distributed datasets. *Bioinformatics* **26**, 2204–2207 (2010).
111. Zhao, H. et al. CrossMap: a versatile tool for coordinate conversion between genome assemblies. *Bioinformatics* **30**, 1006–1007 (2014).
112. Pope, B. D. et al. Topologically associating domains are stable units of replication-timing regulation. *Nature* **515**, 402–405 (2014).


## Acknowledgements

We thank the Rada-Iglesias laboratory members for insightful comments and critical reading of the manuscript. T.P. is supported by a doctoral fellowship from the DAAD (Germany). V.S.-G. is supported by a doctoral fellowship from the University of Cantabria (Spain). Work in the Rada-Iglesias laboratory was supported by the EMBO Young Investigator Programme; CMMC intramural funding (Germany); the German Research Foundation (DFG) (Research Grant no. RA 2547/2-1); 'Programa STAR-Santander Universidades, Campus Cantabria Internacional de la convocatoria CEI 2015 de Campus de Excelencia Internacional' (Spain); the Spanish Ministry of Science, Innovation and Universities (Research Grant nos. PGC2018-095301-B-I00 and RED2018-102553-T REDEVNEURAL 3.0); and the European Research Council (ERC CoG '*PoisedLogic*'; grant no. 862022). The Landeira laboratory is funded by grants from the Spanish Ministry of Science and Innovation (grant nos. BFU2016-75233-P and PID2019-108108GB-I00) and the Andalusian Regional Government (grant no. PC-0246-2017).

## Author contributions

T.P. and A.R.-I. conceptualized the project. Experimental investigations were performed by T.P., T.E., M.M.-F., H.G.A., P.R., M.M.-S. and E.H. T.P., V.S.-G. and T.B. performed data analyses. T.P. and A.R.-I. wrote, reviewed and edited the manuscript. S.C.-M., W.F.J.v.I., D.L. and A.R.-I. were responsible for obtaining resources. A.R.-I. was responsible for supervision and funding acquisition.

## Competing interests

The authors declare no competing interests.

## Additional information

**Extended data** is available for this paper at https://doi.org/10.1038/s41588-021-00888-x.

**Supplementary information** The online version contains supplementary material available at https://doi.org/10.1038/s41588-021-00888-x.

**Correspondence and requests for materials** should be addressed to A.R.-I.

**Peer review information** *Nature Genetics* thanks Darío Lupiáñez, Robin Andersson and the other, anonymous, reviewer(s) for their contribution to the peer review of this work. Peer reviewer reports are available.

**Reprints and permissions information** is available at www.nature.com/reprints.

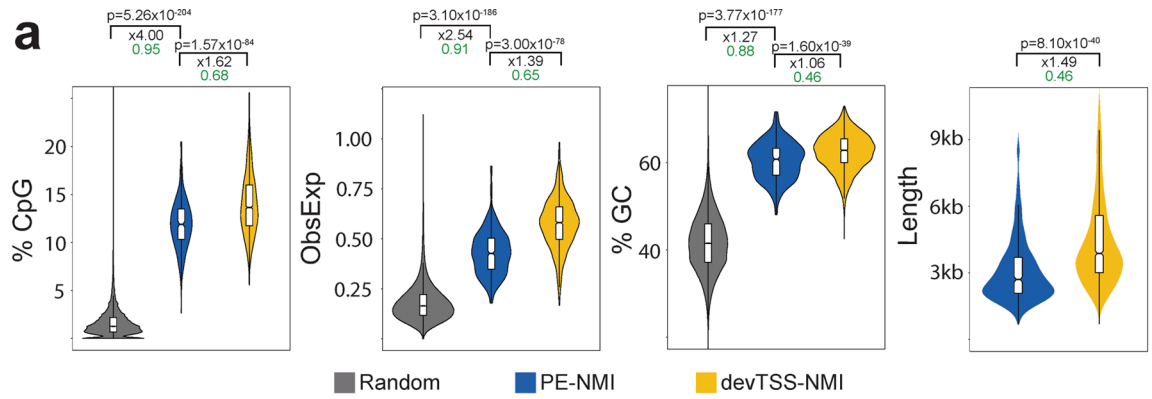


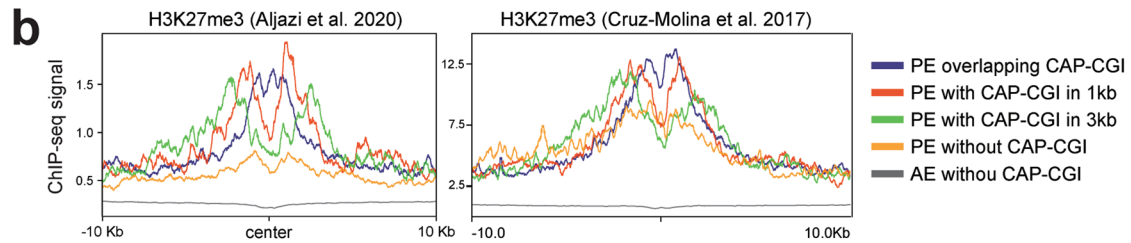


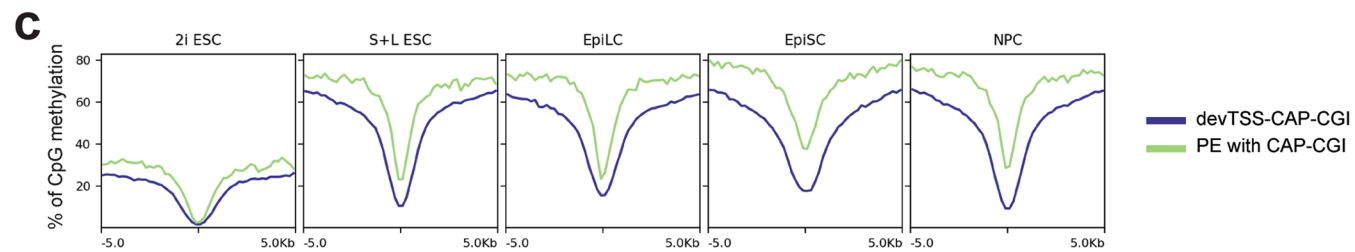


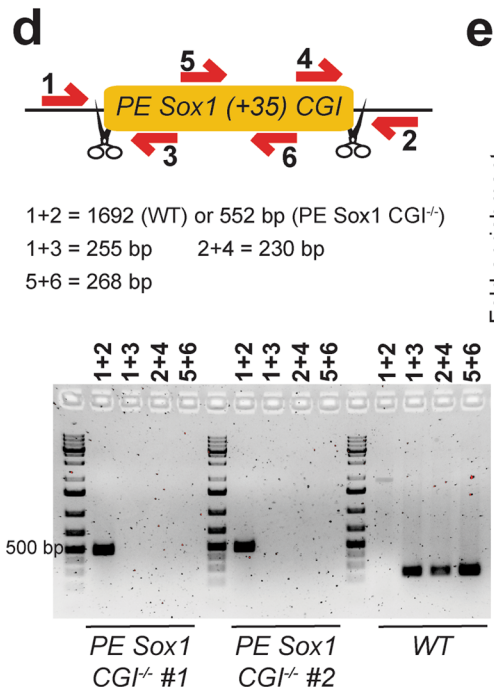


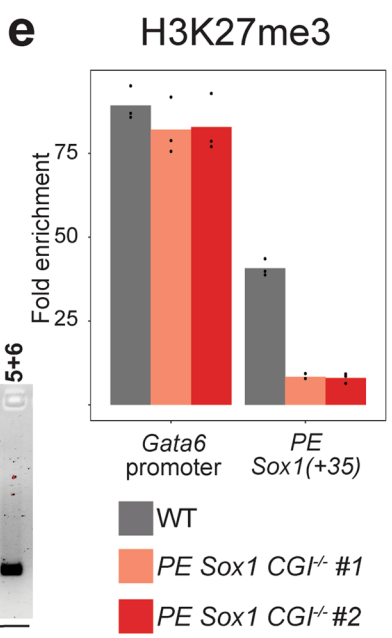


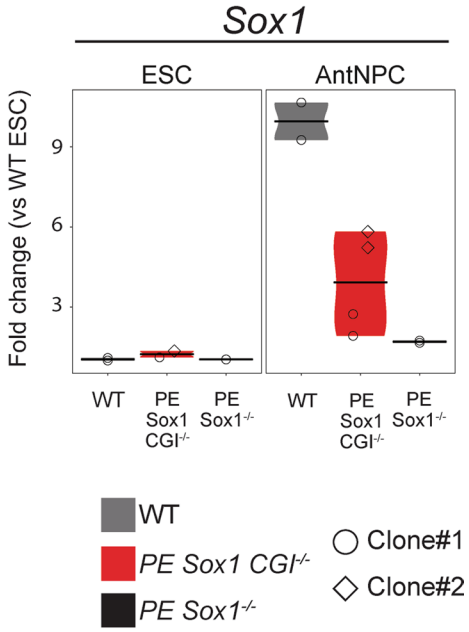


**Extended Data Fig. 1 | See next page for caption.**

**Extended Data Fig. 1 | Genetic and epigenetic features of the oCGIs associated with PEs. a**, Comparison of CpG%, observed/expected CpG ratio, GC% and sequence length between random regions (n = 436000), NMIs associated to *PE-distal* (*PE-NMIs*; n = 345) and NMIs associated to the *devTSS* (*devTSS-NMIs*; n = 1476) (Methods). The p-values were calculated using two-sided unpaired Wilcoxon tests with Bonferroni correction for multiple testing; black numbers indicate median fold-changes; green numbers indicate non-negligible Cliff Delta effect sizes. The coloured area of the violin plot represents the expression values distribution and the center line represents the median. **b**, H3K27me3 ChIP-seq levels[14,24] around: *PE-distal* with overlapping TFBS/p300 peaks and CAP-CGIs (n = 135), *PE-distal* with TFBS/p300 peaks separated by 1bp-1kb from CAP-CGIs (n = 65), *PE-distal* with TFBS/p300 peaks separated by 1-3kb from CAP-CGIs (n = 53), *PE-distal* without CAP-CGIs within 3kb (n = 254) and AEs without CAP-CGI within 3kb (n = 8115). **c**, % of CpG methylation at CAP-CGI associated with *PE-distal* (PE-CAP-CGI; n = 276) and CAP-CGI associated with the TSS of developmental genes (devTSS-CAP-CGI; n = 1926) in the indicated cell types (Methods). **d**, For the identification of the *PE Sox1(+35)CGI* deletion, primer pairs flanking each of the deletion breakpoints (1 + 3 and 4 + 2), located within the deleted region (5 + 6) or amplifying a large or small fragment depending on the absence or presence of the deletion (1 + 2) were used. **e**, H3K27me3 levels at *PE Sox1(+35)* were measured by ChIP-qPCR in WT ESCs and in n = 2 independent *PE Sox1(+35) CGI*$^{-/-}$ ESCs clones using primers adjacent to the deleted region. The bars display the mean of n = 3 technical replicates (black dots). **f**, Independent biological replicate for the data presented in Fig. 1d. *Sox1* expression was investigated by RT-qPCR in ESCs and AntNPC with the indicated genotypes. n = 2 independent *PE Sox1 CGI*$^{-/-}$ ESC clones (circles and diamonds) and n = 1 *PE Sox1*$^{-/-}$ clone were studied. For each cell line, n = 2 replicates of the AntNPC differentiation were performed. Expression values were normalized to two housekeeping genes (*Eef1a* and *Hprt*) and are presented as fold-changes with respect to WT ESCs. The coloured area of the violin plot represents the expression values distribution and the center line represents the median.

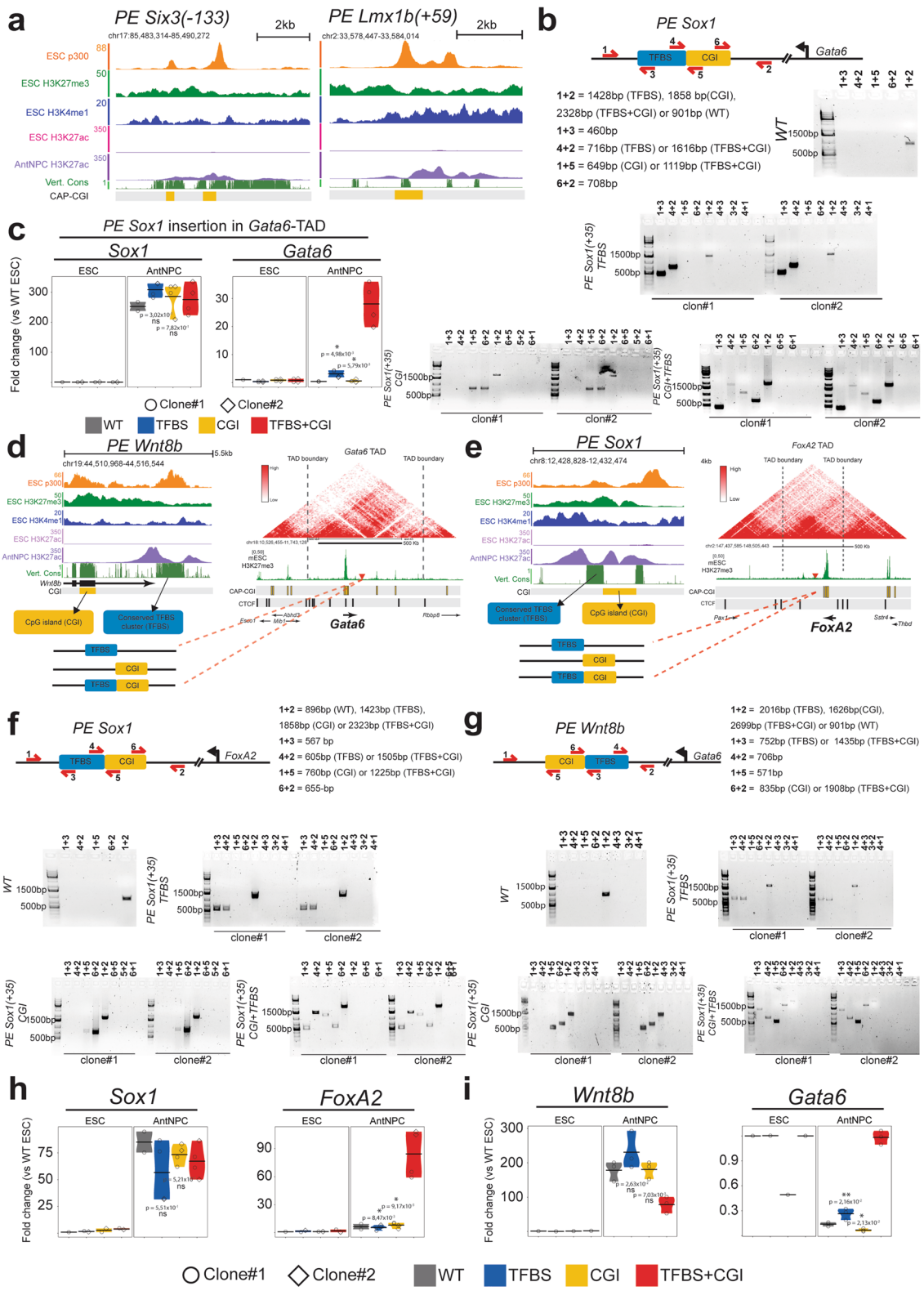


**Extended Data Fig. 2 | See next page for caption.**

**Extended Data Fig. 2 | Engineering of PEs modules within the Gata6-TAD and FoxA2-TAD. a**, Epigenomic and genomic features of two previously characterized PEs[14] (*PE Six3(−133)*; *PE Lmx1b(+59)*) in which the oCGIs overlap with conserved sequences bound by p300 and, thus, likely to contain relevant TFBS. **b**, The different *PE Sox1(+35)* insertions were identified using primer pairs flanking the insertion borders (1+3 and 4+2; 1+5 and 6+2; 1+3 and 6+2), amplifying potential duplications (4+3, 3+2 and 4+1; 6+5, 5+2 and 6+1) and amplifying a large or small fragment depending on the absence or presence of the insertion (1+2), respectively. The PCR results obtained for WT ESCs and for two ESC clonal lines with homozygous insertions of the *PE Sox1(+35)* modules in the *Gata6*-TAD are shown. **c**, Independent biological replicate for the data presented in Fig. 2b. **d-e**, Strategy used to insert the *PE Wnt8b(+21)* (d) or the *PE Sox1(+35)* (e) components into the *Gata6*-TAD (d) or *Foxa2*-TAD (e), respectively. The right panels shows the TADs in which *Gata6* (d) or *Foxa2* (e) are included according to publically available Hi-C data[80,81], with the red triangle indicating the integration site of the PE modules, approximately 100 Kb downstream of *Gata6* (d) or *Foxa2* (e). **f-g**, For identifying the successful insertion of the different *PE Sox1(+35)* (f) or *PE Wnt8b(+21)* (g) modules, primer pairs flanking the insertion borders (1+3 and 4+2; 1+5 and 6+2; 1+3 and 6+2), amplifying potential duplications (4+3, 3+2 and 4+1; 6+5, 5+2 and 6+1) and amplifying a large or small fragment depending on the absence or presence of the insertion (1+2), respectively, were used. The PCR results obtained for two ESC clonal lines with homozygous insertions of the indicated PE modules in the *Foxa2*-TAD (f) or *Gata6*-TAD (g), respectively, are shown. **h-i**, Independent biological replicates for the data shown in Fig. 2c (h) and Fig. 2d (i). In (c), (h) and (i), the expression differences between AntNPCs with the TFBS+CGI module and AntNPCs with the other PE modules were calculated using two-sided non-paired t-tests (**: foldchange>2 & p<0.001; *: foldchange> 2 & p<0.05; ns: not significant; fold-change<2 or p>0.05).

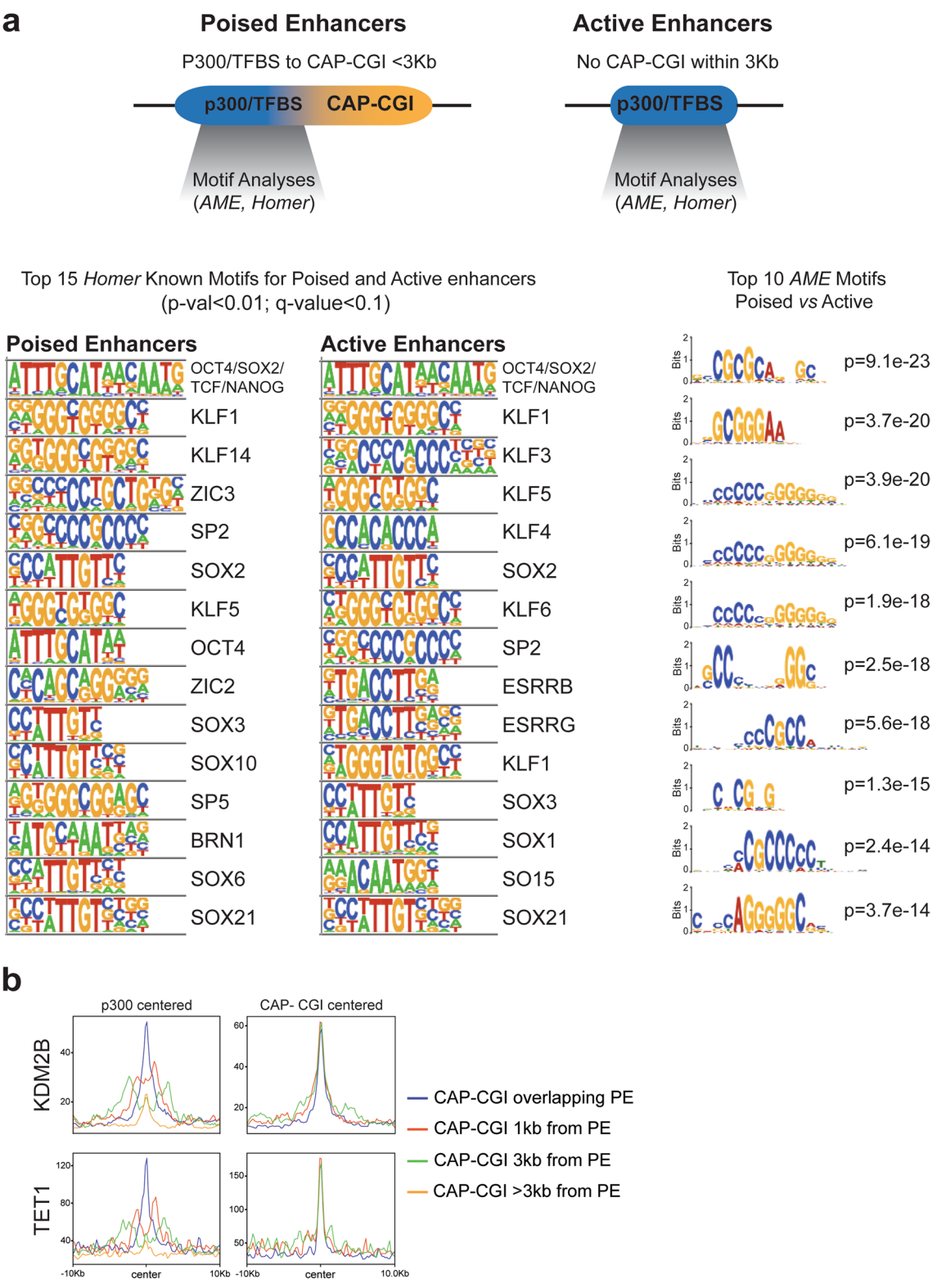


**Extended Data Fig. 3 | PEs are enriched in CpG-rich motifs and are bound by CxxC-domain containing proteins. a**, Comparison of the TF motifs enriched in either PEs with a CAP-CGI in <3kb and active enhancers without CAP-CGIs in <3kb. Motif enrichment analyses were performed with *Homer*[82] (left) and *AME*[107] (right). **b**, ChIP-seq signals for KDM2B[31] (upper panel) and TET1[32] (lower panel) are shown around: *PE-distal* with overlapping TFBS/p300 peaks and CAP-CGIs (n=135), *PE-distal* with TFBS/p300 peaks separated by 1bp-1kb from CAP-CGIs (n=65), *PE-distal* with TFBS/p300 peaks separated by 1-3kb from CAP-CGIs (n=53) and *PE-distal* without CAP-CGIs within 3kb (n=254). ChIP-seq profile plots were generated using either the p300 peaks (left) or the CAP-CGIs (right) associated with the PEs as midpoints.

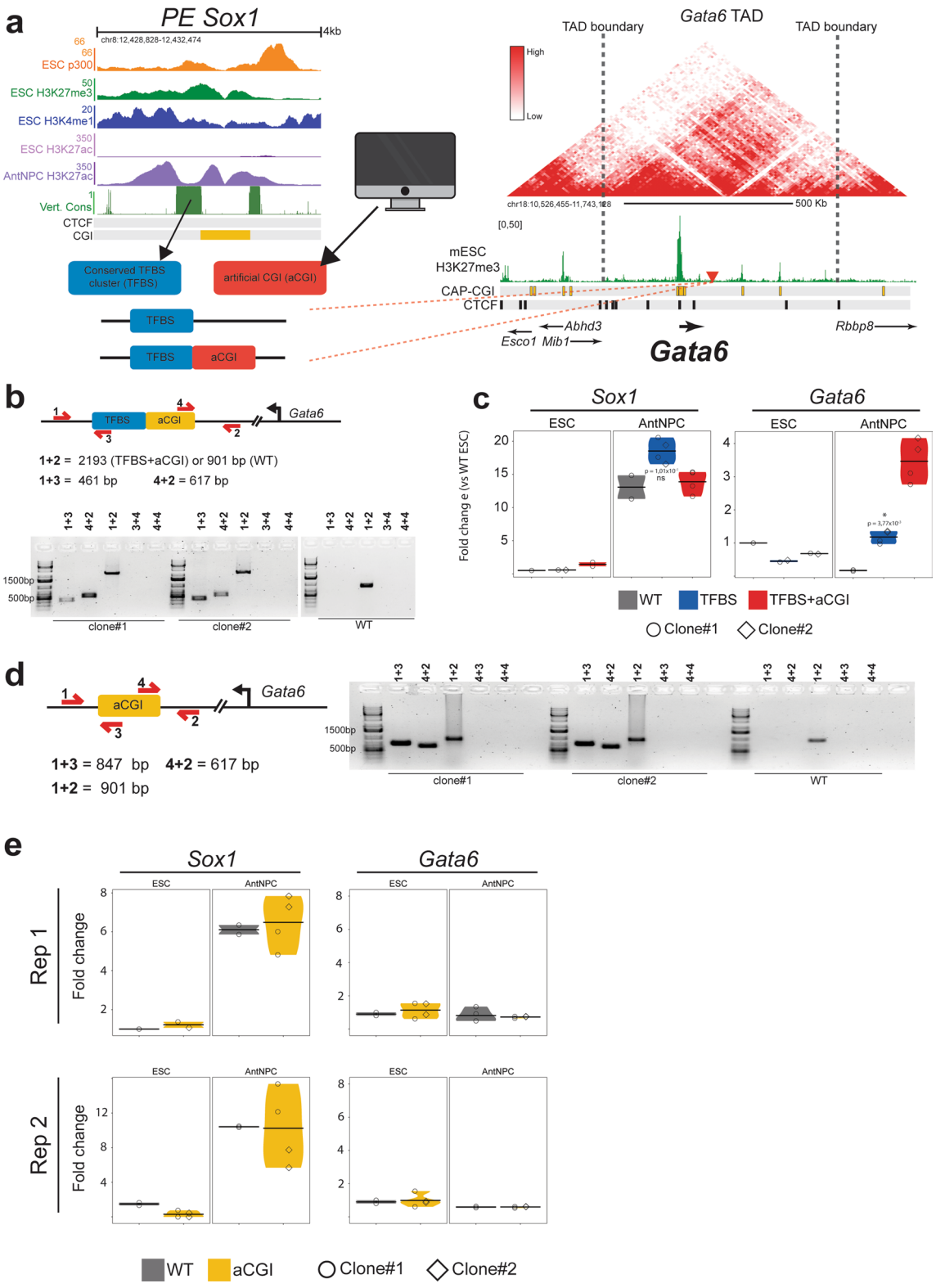


**Extended Data Fig. 4 | See next page for caption.**

**Extended Data Fig. 4 | Engineering of ESC lines containing the *PE Sox1(+35)* TFBS and an artificial CGI within the *Gata6*-TAD. a**, Strategy used to insert the *PE Sox1(+35)TFBS* alone or together with an aCGI into the *Gata6*-TAD. The upper left panel shows the epigenomic and genetic features of the *PE Sox1(+35)*. The lower left panel shows the *PE Sox1(+35)* modules inserted into the *Gata6*-TAD. The right panel shows the *Gata6*-TAD according to publically available Hi-C data[80,81]. The red triangle indicates the integration site of the *PE Sox1(+35)* modules approximately 100 Kb downstream of *Gata6*. **b**, For the identification of the *PE Sox1(+35)TFBS+aCGI* insertion, primer pairs flanking the insertion borders (1+3 and 4+2), amplifying potential duplications (4 + 3 and 4 + 4) and amplifying a large or small fragment depending on the absence or presence of the insertion (1 + 2), respectively, were used. The PCR results obtained for two ESC clonal lines with homozygous insertions of *PE Sox1(+35)TFBS+aCGI* in the *Gata6*-TAD are shown. **c**, Independent biological replicate for the data presented in Fig. 2f. The expression differences between AntNPCs with the TFBS+CGI module and AntNPCs with the other PE modules were calculated using two-sided non-paired t-tests (*: foldchange> 2 & p<0.05; ns: not significant; fold-change<2 or p>0.05). **d**, For the identification of the aCGI insertion alone, primer pairs flanking the insertion borders (1 + 3 and 4 + 2), amplifying potential duplications (4 + 3 and 4 + 4) and amplifying a large or small fragment depending on the absence or presence of the insertion (1 + 2), respectively, were used. The PCR results obtained from two ESC clonal lines with heterozygous insertions of aCGI in the *Gata6*-TAD are shown. **e**, The expression of *Gata6* and *Sox1* was measured by RT-qPCR in cells that were either WT or heterozygous for the aCGI insertion in the *Gata6*-TAD (two different clones; circles and diamonds). For each cell line, n = 2 replicates of the AntNPC differentiation were performed. The results obtained in n = 2 independent biological replicates are presented in each panel (Rep1 and Rep2).

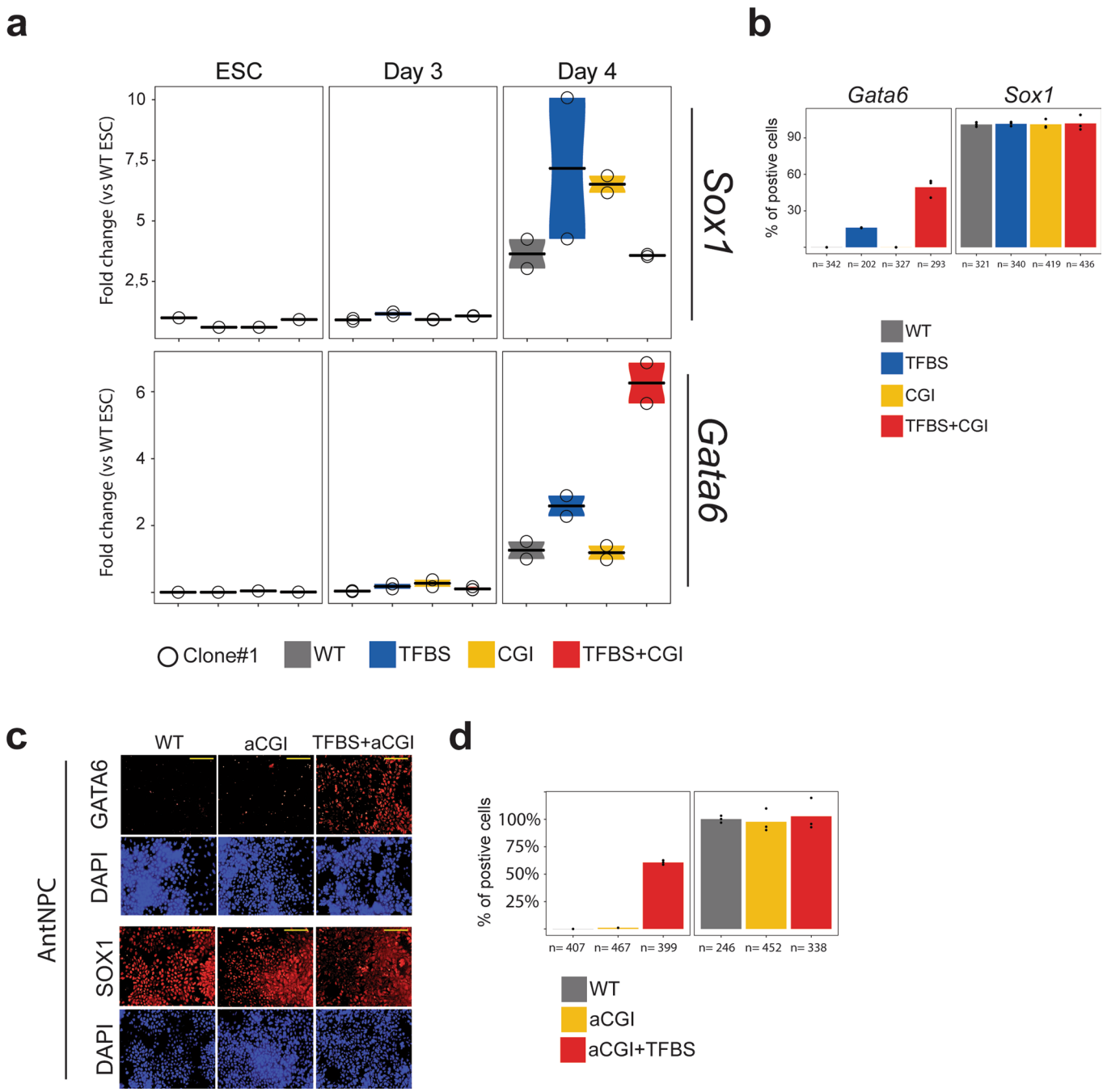


**Extended Data Fig. 5 | *Gata6* expression patterns in cell lines with the *PE Sox1(+35)* modules inserted within the *Gata6*-TAD. a**, *Gata6* and *Sox1* expression was measured by RT-qPCR in ESCs and at intermediate stages of AntNPC differentiation (Day 3 and Day 4). The analysed cells were either WT or homozygous for the insertions of the different *PE Sox1(+35)* modules within the *Gata6*-TAD. For the cells with the PE module insertions, n = 1 clonal cell line was studied. For each cell line, n = 2 replicates of the AntNPC differentiation were performed. Expression values were normalized to two housekeeping genes (*Eef1a* and *Hprt*) and are presented as fold-changes with respect to WT ESCs. ***b***, Quantification of cells expressing GATA6 or SOX1 according to immunofluorescence assays as the ones shown in Fig. 2g. The analysed cells were either WT of homozygous for the insertions of the different *PE Sox1(+35)* modules within the *Gata6*-TAD. **c**, The expression patterns of GATA6 (upper panel) and SOX1 (lower panel) were investigated by immunofluorescence in WT ESCs or AntNPCs that were either WT, homozygous for the insertion of the *PE Sox1(+35)TFBS + aCGI* in the *Gata6*-TAD or heterozygous for the insertion of the aCGI alone in the *Gata6*-TAD. Nuclei were stained with DAPI. Scale bar = 100μm. **d**, Quantification of cells expressing GATA6 or SOX1 according to the immunofluorescence assays described in (c). In (b) and (d), the bars display the mean of n = 3 technical replicates (black dots).

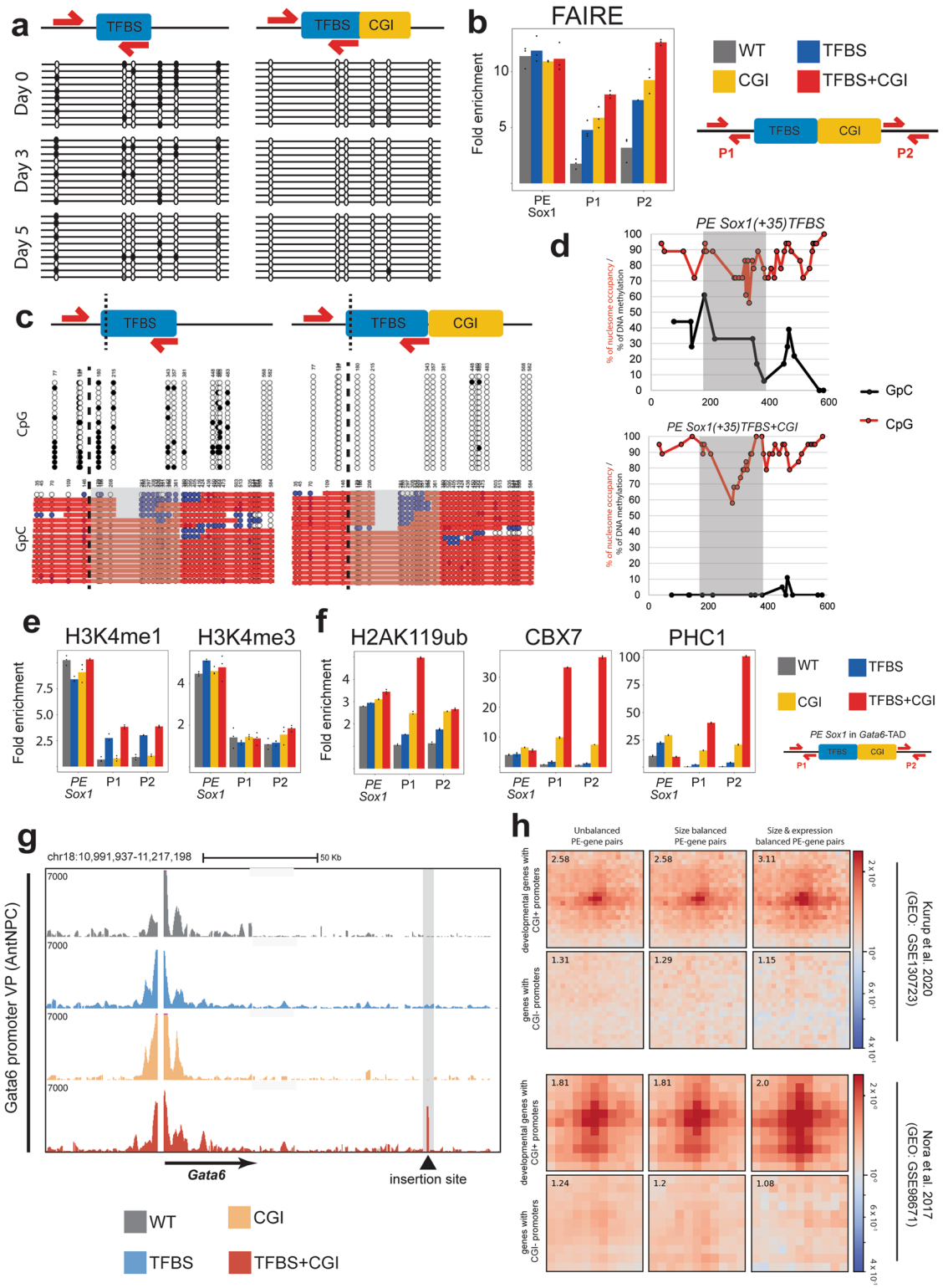


**Extended Data Fig. 6 | See next page for caption.**

**Extended Data Fig. 6 | Epigenetic and topological characterization of the *Gata6*-TAD cell lines. a**, Bisulfite sequencing data presented in Fig. 3a for the indicated *Gata6*-TAD cell lines. The circles correspond to individual CpG dinucleotides located within the TFBS module. Unmethylated CpGs are shown in white, methylated CpGs in black and not-covered CpGs in gray. **b**, Chromatin accessibility at the endogenous *PE Sox1(+35)* and the *Gata6*-TAD insertion site (P1 and P2) were measured by FAIRE-qPCR in cells with the indicated genotypes. **c**, DNA methylation and nucleosome occupancy at the TFBS were simultaneously analyzed by NOMe-PCR in the indicated *Gata6*-TAD ESC lines. In the upper panels, the black and white circles represent methylated or unmethylated CpG sites, respectively. In the lower panels, the blue or white circles represent accessible or inaccessible GpC sites for the GpC methyltransferase, respectively. Red bars represent inaccessible regions large enough to accommodate a nucleosome. The dotted line indicates where the TFBS starts. The grey shaded area represents a nucleosome-depleted region. **d**, Scatter plots showing population-averaged nucleosome occupancy (red) and DNA methylation (black) levels within the TFBS in the indicated *Gata6*-TAD ESC lines. The grey shaded area represents a nucleosome depleted region. **e-f**, H3K4me1, H3K4me3, H2AK119ub, CBX7 and PHC1 levels at the endogenous *PE Sox1(+35)* and the *Gata6*-TAD insertion site (P1 and P2) were measured by ChIP-qPCR in cells with the indicated genoytpes. ChIP-qPCR signals were calculated as described in Fig. 3. **g**, 4C-seq experiments were performed using the *Gata6* promoter as a viewpoint in AntNPC with the indicated genotypes. **h**, Pile-up plots showing average Hi-C[7,52] signals in ESC between two groups of PE-gene pairs: PEs and developmental genes with CGI-rich promoters; PEs and genes with CGI-poor promoters. For each PE-gene pair, both the PE and the gene were located within the same TAD. Left panels include all the considered PE-gene pairs (n = 401 pairs for developmental genes; n = 900 for CGI-poor promoters; middle panels includes PE-gene pairs with the same genomic size in the two groups (n = 401 pairs); right panels consist of PE-gene pairs with the same genomic size and genes with expression levels <1 FPKM[9] (n = 290 pairs) (Methods).

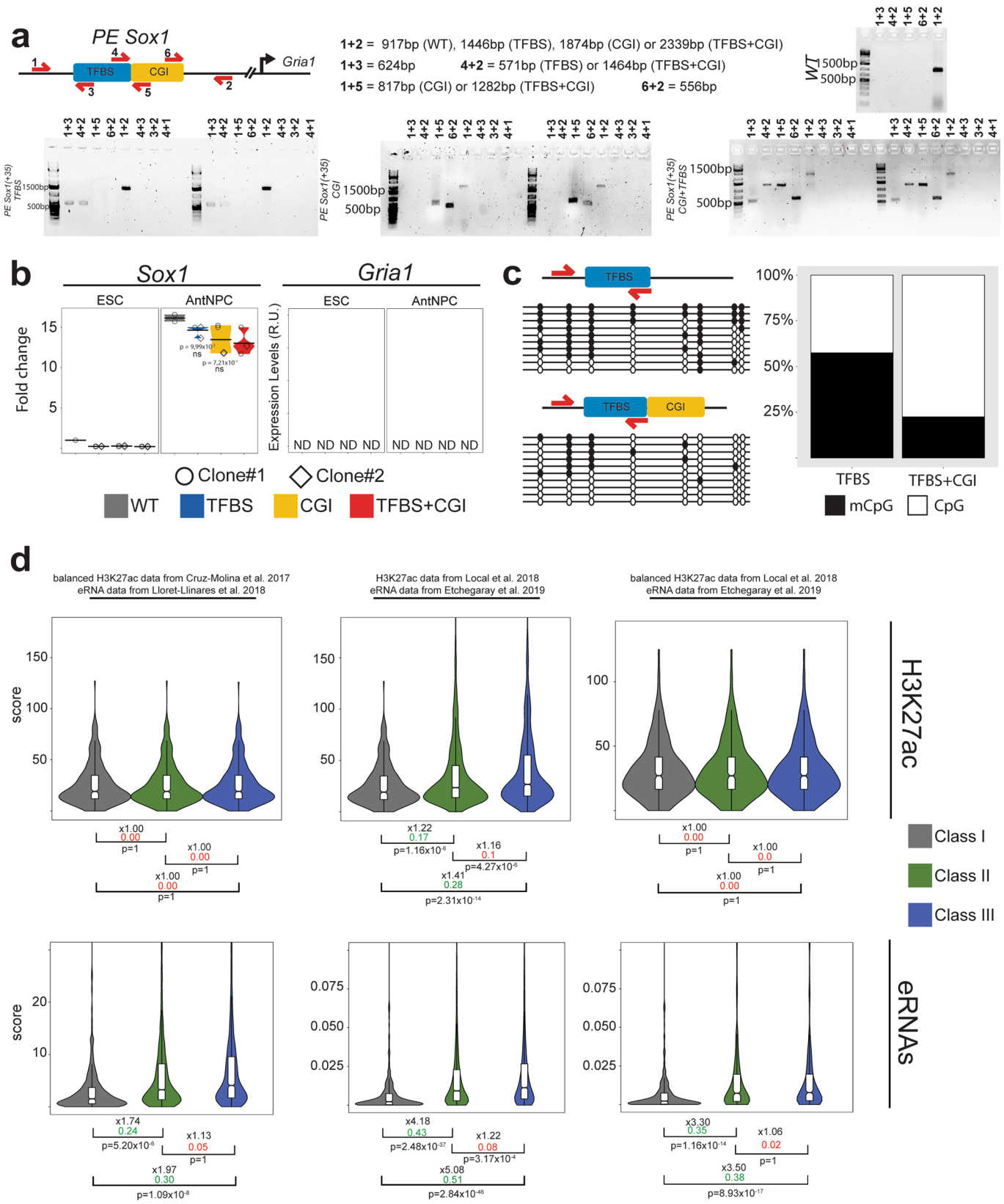


**Extended Data Fig. 7 | See next page for caption.**

**Extended Data Fig. 7 | Generation of cell lines with engineered *PE Sox1(+35)* modules within the *Gria1-TAD* and global characterization of H3K27ac and eRNA levels at active enhancers. a**, ESC clonal lines with insertions of the different *PE Sox1(+35)* modules were identified using primer pairs flanking the insertion borders (1 + 3 and 4 + 2; 1 + 5 and 6 + 2; 1 + 3 and 6 + 2), amplifying potential duplications (4 + 3, 3 + 2 and 4 + 1; 6 + 5, 5 + 2 and 6 + 1) and amplifying a large or small fragment depending on the absence or presence of the insertion (1 + 2), respectively. The PCR results obtained for WT ESCs or two ESC clonal lines with homozygous insertions of the different *PE Sox1(+35)* modules in the *Gria1*-TAD are shown. **b**, Independent biological replicate for the data presented in Fig. 4b. The expression differences between AntNPCs with the TFBS + CGI module and AntNPCs with the other PE modules were calculated using two-sided non-paired t-tests (ns: not significant; fold-change<2 or p>0.05). **c**, Bisulfite sequencing analyses of ESC lines with the indicated *PE Sox1(+35)* modules inserted in the *Gria1*-TAD. The circles correspond to individual CpG dinucleotides located within the TFBS: unmethylated CpGs (white), methylated CpGs (black) and not-covered CpGs (gray) are shown. The plot on the right summarizes the DNA methylation levels measured within the TFBS in the indicated ESC lines. **d**, Active enhancers (AEs) identified in ESCs based on the presence of distal H3K27ac peaks were classified into three categories (Methods): Class I (AEs in TADs containing only poorly expressed genes; n = 271(left); n = 340 (middle, right); Class II (AEs in TADs with at least one highly expressed gene; n = 271(left); n = 2353(middle); n = 340(right)); Class III (AEs whose closest genes in the same TAD is highly expressed; n = 271(left); n = 1262(middle); n = 340(right)). The violin plots show the H3K27ac and eRNA levels in ESC for each AE category. P-values were calculated using unpaired Wilcoxon tests with Bonferroni correction for multiple testing; the numbers in black indicate the median fold-changes between the indicated groups; the coloured numbers correspond to Cliff Delta effect sizes: negligible (red) and non-negligible (green). In the left and right panels, eRNA levels for the three enhancers classes are compared after correcting for H3K27ac differences (Methods).

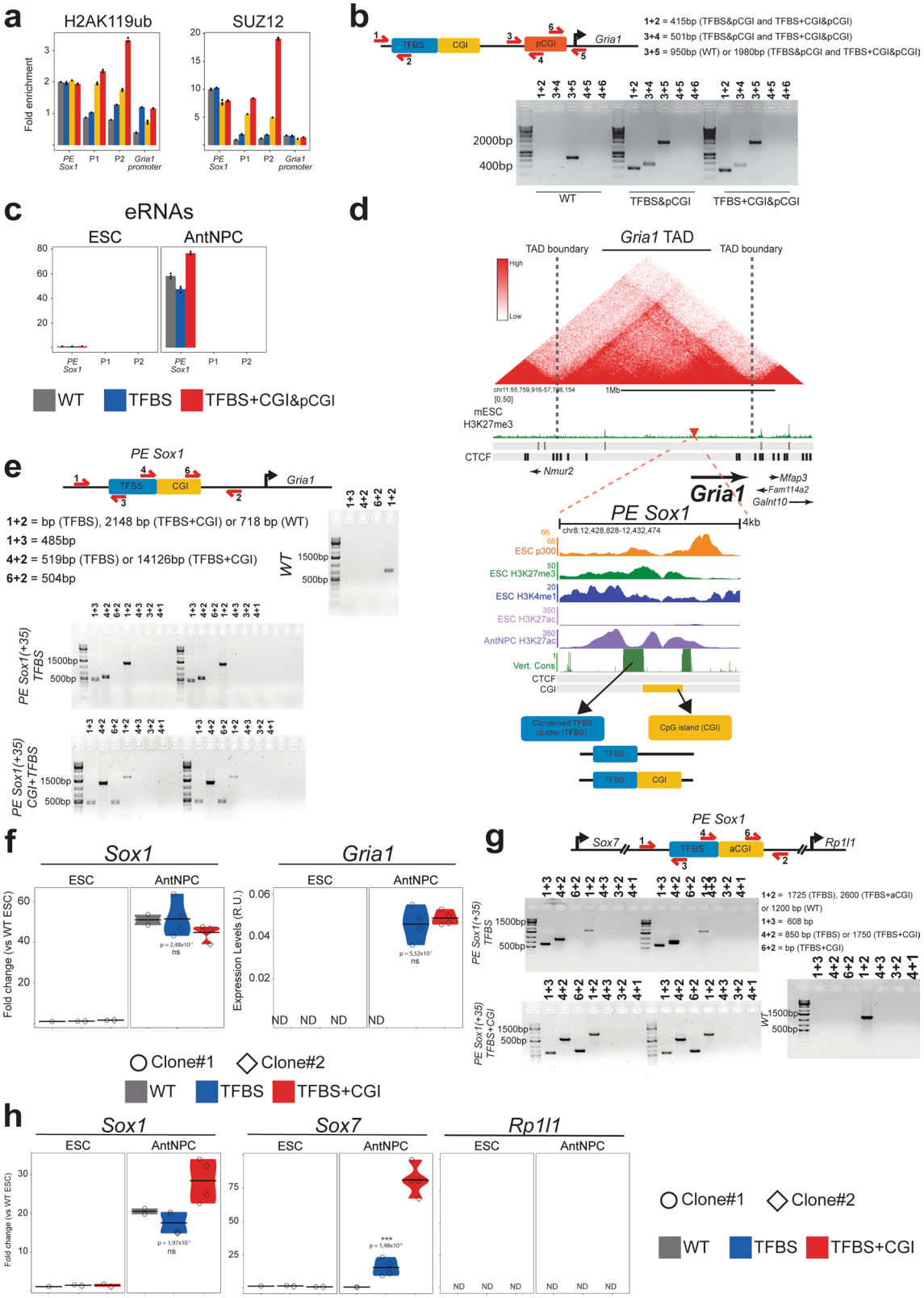


**Extended Data Fig. 8 | See next page for caption.**

**Extended Data Fig. 8 | Generation and characterization of cell lines with PE insertions at the *Gria1* and *Sox7/Rp1l1* TADs. a**, H2AK229ub and SUZ12 levels at the endogenous *PE Sox1(+35)*, the *Gria1* promoter and the *Gria1*-TAD insertion site (P1 and P2; Fig. 4d) were measured by ChIP-qPCR in ESCs with the indicated genotypes. ChIP-qPCR signals were calculated as in Fig. 3. **b**, ESC clonal lines in which a pCGI was inserted 380bp upstream of the *Gria1*-TSS in cells with the indicated *PE Sox1(+35)* modules 100Kb upstream from *Gria1* were identified using the indicated primer pairs. PCR results for clonal ESC lines with the indicated double homozygous insertions are shown. **c**, eRNA levels at the endogenous *PE Sox1(+35)* and the *Gria1*-TAD insertion site (P1 and P2) were measured by RT-qPCR in cells with the indicated genotypes. Expression values were calculated as in Fig. 3. **d**, Strategy to insert the indicated *PE Sox1(+35)* modules 380bp upstream (red triangle) of the *Gria1*-TSS. **e**, ESC clonal lines with the *PE Sox1(+35)* modules 380bp upstream of the *Gria1*-TSS were identified using the indicated primer pairs. PCR for ESC clonal lines with homozygous insertions of the indicated *PE Sox1(+35)* modules are shown. **f**, Independent biological replicate for the data presented in Fig. 5e. **g**, ESC clonal lines with the *PE Sox1(+35)* modules within the *Sox7/Rp1l1*-TAD were identified using primers flanking the insertion borders (1+3 and 4+2; 1+3 and 6+2), amplifying potential duplications (4+3, 3+2 and 4+1) and amplifying a large or small fragment depending on the absence or presence of the insertion (1+2), respectively. PCR results for ESC clonal lines with homozygous insertions of the indicated *PE Sox1(+35)* modules are shown. **h**, Independent biological replicate for the data presented in Fig. 5g. In (a) and (c), the bars display the mean of n=3 technical replicates (black dots). In (f) and (h), the expression differences between AntNPCs with the TFBS+CGI module or the other PE modules were calculated using two-sided non-paired t-tests (***: foldchange> 2 & $p<0.0001$; ns: not significant; fold-change<2 or $p>0.05$).

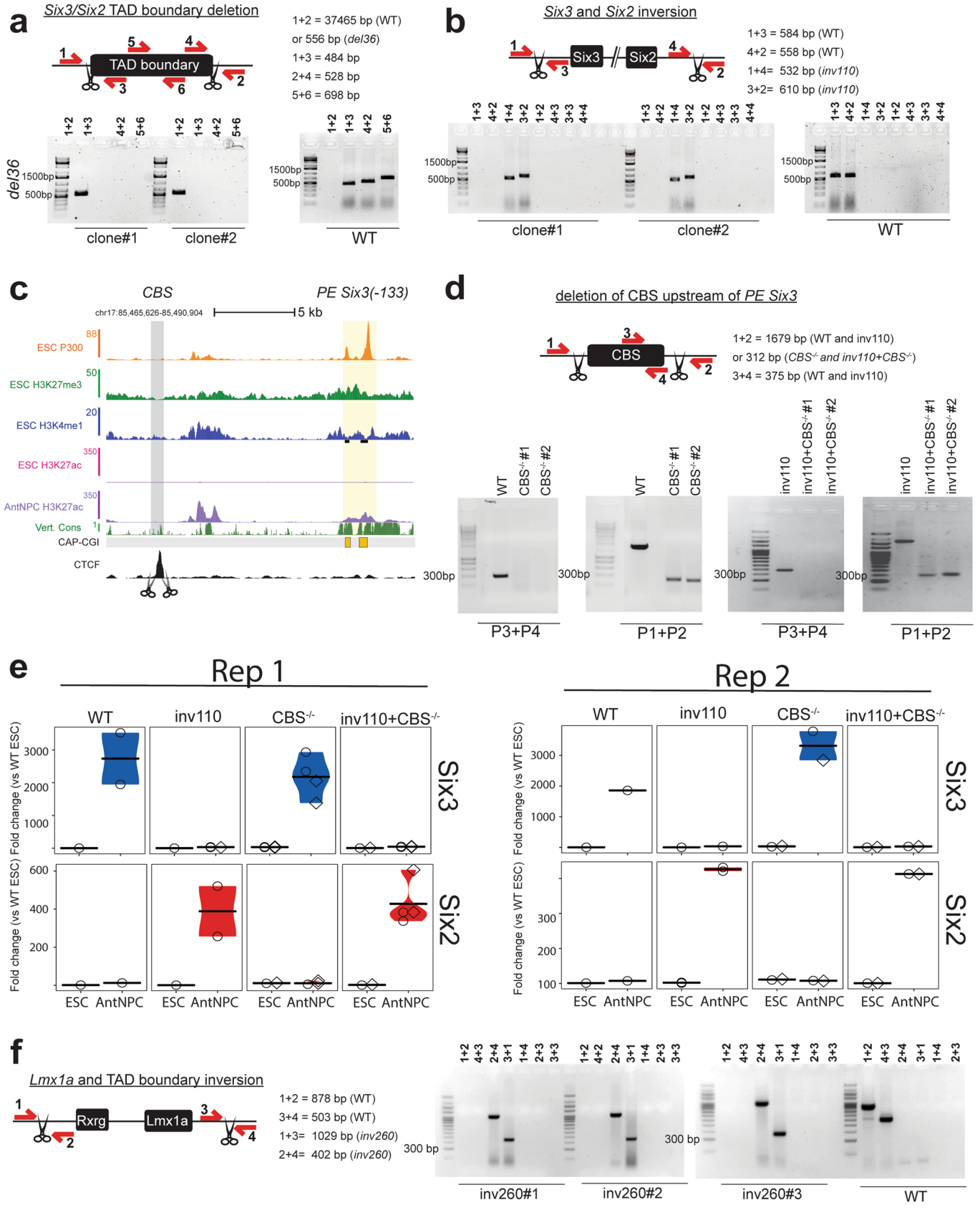


**Extended Data Fig. 9 | See next page for caption.**

**Extended Data Fig. 9 | Generation of ESC lines with structural variants. a**, ESC lines with the *Six3/Six2* TAD boundary deletion were identified using primers flanking the deleted region (1+3 and 4+2), amplifying the deleted fragment (5+6) and amplifying a large or small fragment depending on the absence or presence of the deletion (1+2), respectively. The PCR results for two ESC clonal lines with 36Kb homozygous deletions (*del36*) are shown. **b**, ESC lines with the *Six3/Six2* inversion were identified using primer pairs flanking the inverted region (1+3, 4+2, 1+4 and 3+2) and amplifying potential duplications (4+3, 3+3 and 4+4). The PCR results for two ESC clonal lines with 110Kb homozygous inversions (*inv110*) are shown. **c**, Epigenomic and genetic features of a CTCF binding site[112] (CBS; highlighted in grey) located upstream of the *PE Six1(−133)* (highlighted in yellow). **d**, ESC lines with the CBS deletion were identified using primers flanking the deleted region (1+2) or located in the CBS (3+4). The PCR results for two ESC clonal lines with homozygous CBS deletions are shown. **e**, The expression of *Six3* and *Six2* was measured by RT-qPCR in cells with the indicated genotypes. For each of the engineered structural variants, n = 2 independent clonal cell lines were generated (circles and diamonds). In each plot, the number of circles and/or diamonds corresponds to the number of AntNPC differentiations performed. The results obtained in n = 2 independent biological replicates are presented in each panel (Rep1 and Rep2). Expression values are presented as fold-changes with respect to WT ESCs. **f**, ESC lines with the *Lmx1a*-TAD boundary inversion were identified using primers flanking the inverted region (1+3, 4+2, 1+4 and 3+2) and amplifying potential deletions (1+4) or duplications (4+3, 3+3 and 4+4). The PCR results for three ESC clonal lines with 260 Kb homozygous inversions (*inv260*) are shown.

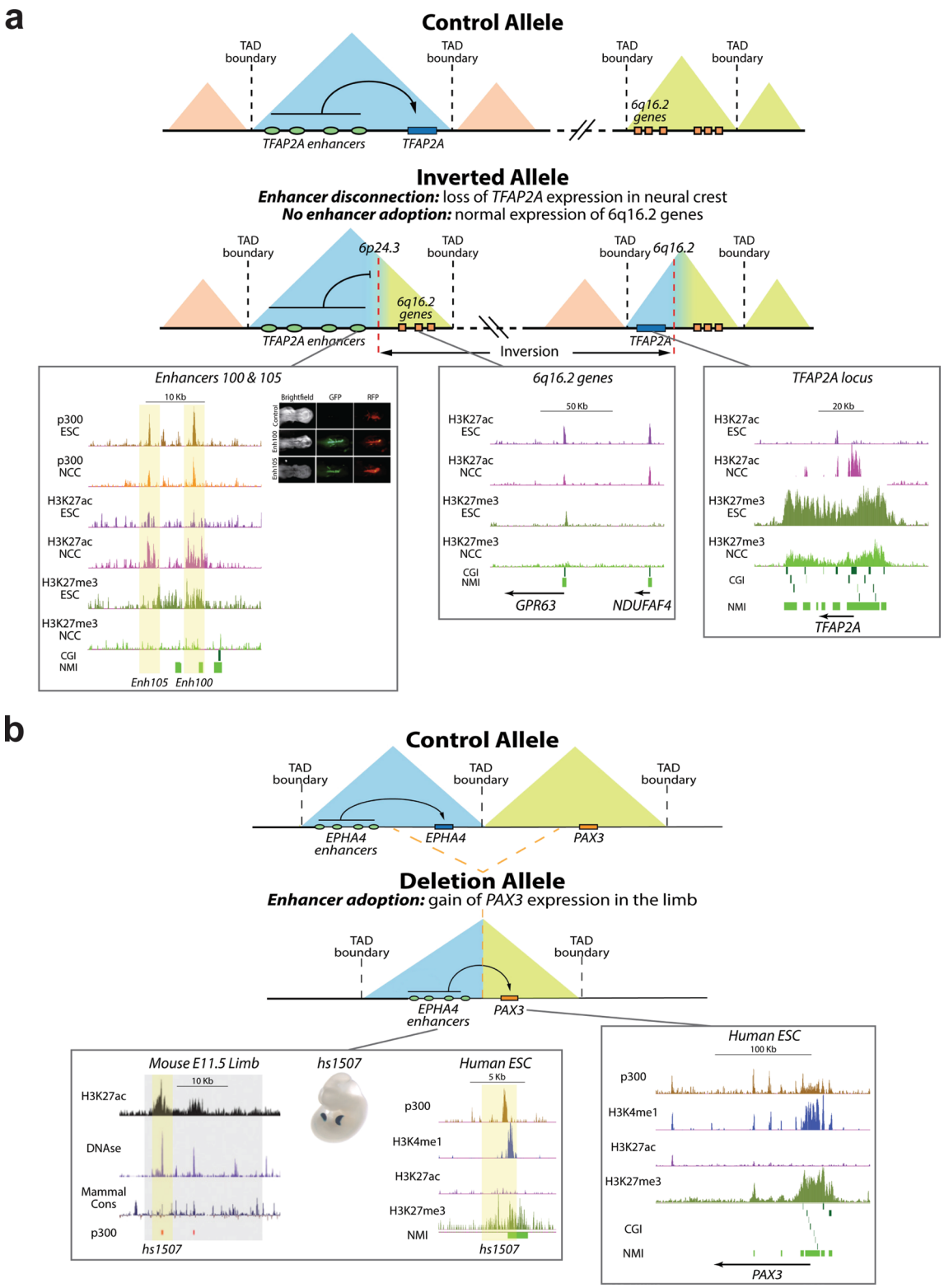


**Extended Data Fig. 10 | See next page for caption.**

**Extended Data Fig. 10 | Examples of human congenital diseases caused by structural variants that disrupt developmental loci with PE-associated oCGIs. a**, Upper panel: heterozygous inversion in a patient with Branchio-oculo-facial syndrome (BOFS)[5]. Lower panel: epigenomic and genetic features of *TFAP2A* neural crest (NC) cognate enhancers (left), 6q16.2 genes (middle) and *TFAP2A* (right). In the lower left panel, enhancer reporter assays in chicken embryos are shown for two representative *TFAP2A* enhancers[5]. Computational CGI and NMIs are represented as green rectangles. The inversion places one *TFAP2A* allele into a novel TAD and impairs its normal expression in NC cells due to the physical disconnection from its enhancers. *TFAP2A* has a promoter with a large CGI cluster and marked with a broad H3K27me3 domain in ESCs. Some *TFAP2A* NC enhancers are associated with oCGIs and marked with H3K27me3 in ESCs. Moreover, this inversion places genes originally found within the 6q16.2 locus in proximity of the *TFAP2A* NC enhancers within a shuffled domain. The promoters of these 6q16.2 genes (i.e *GPR63* and *NDUFAF4)* contain a short CGI centered on their TSSs. In agreement with our findings, none of the 6q16.2 genes is responsive to the *TFAP2A* NC enhancers[5]. **b**, Upper panel: deletion found in families with brachydactyly involving a TAD boundary located between the *EPHA4* and the *PAX3* loci[63]. Lower panel: epigenomic and genetic features of the *Epha4* cognate enhancers in the mouse E11.5 limb (left) and in human ESCs (right). Representative reporter assay in E11.5 mouse embryos for the hs1507 element is shown in the middle[63]. The deletion includes *EPHA4*, a gene highly expressed in the developing limb, and the TAD boundary separating the *EPHA4* and *PAX3* TADs. As a result, enhancers that control *EPHA4* expression in the limb establish ectopic interactions with *PAX3* (that is enhancer adoption) and strongly induce its expression in the limb. The *PAX3* promoter contains a large CGI cluster and is marked with H3K27me3 in ESCs, while one of the major *EPHA4* enhancers (hs1507) is associated with an oCGI and is marked with H3K27me3 in ESCs. The high responsiveness of *PAX3* to the *EPHA4* enhancers is in agreement with our findings.

nature research

Corresponding author(s): Alvaro Rada-Iglesias

Last updated by author(s): May 11, 2021

# Reporting Summary

Nature Research wishes to improve the reproducibility of the work that we publish. This form provides structure for consistency and transparency in reporting. For further information on Nature Research policies, see our Editorial Policies and the Editorial Policy Checklist.

## Statistics

For all statistical analyses, confirm that the following items are present in the figure legend, table legend, main text, or Methods section.

| n/a | Confirmed | |
|---|---|---|
| ☐ | ☒ | The exact sample size (*n*) for each experimental group/condition, given as a discrete number and unit of measurement |
| ☐ | ☒ | A statement on whether measurements were taken from distinct samples or whether the same sample was measured repeatedly |
| ☐ | ☒ | The statistical test(s) used AND whether they are one- or two-sided<br>*Only common tests should be described solely by name; describe more complex techniques in the Methods section.* |
| ☒ | ☐ | A description of all covariates tested |
| ☒ | ☐ | A description of any assumptions or corrections, such as tests of normality and adjustment for multiple comparisons |
| ☐ | ☒ | A full description of the statistical parameters including central tendency (e.g. means) or other basic estimates (e.g. regression coefficient) AND variation (e.g. standard deviation) or associated estimates of uncertainty (e.g. confidence intervals) |
| ☐ | ☒ | For null hypothesis testing, the test statistic (e.g. *F*, *t*, *r*) with confidence intervals, effect sizes, degrees of freedom and *P* value noted<br>*Give P values as exact values whenever suitable.* |
| ☒ | ☐ | For Bayesian analysis, information on the choice of priors and Markov chain Monte Carlo settings |
| ☒ | ☐ | For hierarchical and complex designs, identification of the appropriate level for tests and full reporting of outcomes |
| ☐ | ☒ | Estimates of effect sizes (e.g. Cohen's *d*, Pearson's *r*), indicating how they were calculated |

*Our web collection on statistics for biologists contains articles on many of the points above.*

## Software and code

Policy information about availability of computer code

| | |
|---|---|
| Data collection | RT-qPCR: Light Cycler 480II<br>HiSeq 2500 sequencer (Illumina) |
| Data analysis | NOMePlot web app tool 0.80<br>EMBOSS Cpgplot 2019<br>bedtools 2.28.0<br>FastQC 0.11.9<br>MultiQC 1.10.1<br>trimmomatic 0.40<br>cutadapt 1.18<br>Bowtie2 2.4.2<br>SAMtools 1.12<br>MACS2 2.2.7.1<br>inflection R package 1.3.5<br>BSgenome 3.12<br>deepTools 3.0.2<br>MatchIT 4.1.0<br>effsize R package 0.8.1<br>hic2cool software 0.8.3<br>Homer 4.11<br>Seqpos 0.1.0<br>AME 5.3.3 |

BIsmark 0.22.3

For manuscripts utilizing custom algorithms or software that are central to the research but not yet described in published literature, software must be made available to editors and reviewers. We strongly encourage code deposition in a community repository (e.g. GitHub). See the Nature Research guidelines for submitting code & software for further information.

## Data

Policy information about availability of data

All manuscripts must include a data availability statement. This statement should provide the following information, where applicable:

- Accession codes, unique identifiers, or web links for publicly available datasets
- A list of figures that have associated raw data
- A description of any restrictions on data availability

All the genomic data is available in GEO under the accession number GSE156465.
Public available data used: GSE89209, GSM2360929, GSM2808655, GSM2808669, GSE115713, GSE130691, GSM3752487, GSM3752488, GSM2644945, GSM2644946, GSE130723, GSE98671, GSE157748, GSE89209, GSM4774518, GSM4774519, GSM2788888, GSM2788889, GSM2788890

# Field-specific reporting

Please select the one below that is the best fit for your research. If you are not sure, read the appropriate sections before making your selection.

☒ Life sciences ☐ Behavioural & social sciences ☐ Ecological, evolutionary & environmental sciences

For a reference copy of the document with all sections, see nature.com/documents/nr-reporting-summary-flat.pdf

# Life sciences study design

All studies must disclose on these points even when the disclosure is negative.

| | |
|---|---|
| Sample size | For all the transgenic ESC lines we generated at least two clonal lines with the same genotype. Taking into account the amount of different cell lines generated and that the clones from the same cell line were always responding in a very similar manner, we decided to keep a minimum of two clones per investigated genotype. |
| Data exclusions | No data was excluded |
| Replication | All experiments were performed independently at least twice and all the attempts at data replication were successful. The exact number of repicates is described in the corresponding figure legends. |
| Randomization | Randomization was not relevant for our study as the sample sizes of the different experiments were too small for randomization. |
| Blinding | The investigators were not blinded to allocation during experiments and outcome assessment. There was one person in charge of generating and characterizing all the transgenic cell lines and we did not have additional personal that could be solely in charge of analyzing the data. Blinding is typically used with randomization and large sample sizes, which, as stated before, does not apply to our experiments. |

# Reporting for specific materials, systems and methods

We require information from authors about some types of materials, experimental systems and methods used in many studies. Here, indicate whether each material, system or method listed is relevant to your study. If you are not sure if a list item applies to your research, read the appropriate section before selecting a response.

### Materials & experimental systems

| n/a | Involved in the study |
|---|---|
| ☐ | ☒ Antibodies |
| ☐ | ☒ Eukaryotic cell lines |
| ☒ | ☐ Palaeontology and archaeology |
| ☒ | ☐ Animals and other organisms |
| ☒ | ☐ Human research participants |
| ☒ | ☐ Clinical data |
| ☒ | ☐ Dual use research of concern |

### Methods

| n/a | Involved in the study |
|---|---|
| ☒ | ☐ ChIP-seq |
| ☒ | ☐ Flow cytometry |
| ☒ | ☐ MRI-based neuroimaging |

## Antibodies

| | |
|---|---|
| Antibodies used | Antibody Source ID Application Dilution<br><br>H3K4me1 Active Motif 39297 ChIP-qPCR 3 µl |

H3K4me3 Active Motif 39159 ChIP-qPCR 3 µl
H3K27ac Active Motif 39133 ChIP-qPCR 3 µl
H3K27me3 Active Motif 39155 ChIP-qPCR 3 µl
H2AK119ub Cell Signaling Technology 8240S ChIP-qPCR 3 ul
P300 Active Motif 61401 ChIP-qPCR ChIP-qPCR 10 ul

RNAP2 Active Motif 39097 ChIP-qPCR 10 ul
MED1 Bethyl Laboratories A300-793A ChIP-qPCR 10 ul
RING1B Active Motif 39663 ChIP-qPCR 10 ul
SUZ12 Abcam ab12073 ChIP-qPCR 10 ul
CBX7 Abcam ab21873 ChIP-qPCR 10 ul
PHC1 Cell Signaling Technology 13768S ChIP-qPCR 10 ul

GATA6 R&D systems AF1700 Immunofluorescence 8ul/mL
SOX1 R&D systems AF3369 Immunofluorescence 8ul/mL
Donkey anti-Goat IgG Alexa Fluor Plus 488 Invitrogen A32814 1 ul/mL
Donkey anti-Goat IgG Alexa Fluor Plus 594 Invitrogen A32758 1 ul/mL

Validation

H3K4me3, H3K27ac and H3K27me3 antibodies were validated in: Cruz-Molina, S. et al. PRC2 Facilitates the Regulatory Topology Required for Poised Enhancer Function during Pluripotent Stem Cell Differentiation. Cell Stem Cell 20, 1–17 (2017).
H2AK119ub antobody was validated in: Gao Z et al., PCGF homologs, CBX proteins, and RYBP define functionally distinct PRC1 family complexes. Mol Cell. 3. 344-56 (2012).
P300 antibody was validated by the manufacturer: "ChIP was performed using the ChIP-IT® High Sensitivity Kit (Cat. No. 53040) with chromatin from 4.5 million LNCaP cells and 5 µl of p300 antibody. ChIP DNA was sequenced on the Illumina HiSeq and 15 million sequence tags were mapped to identify p300 binding sites. p300 along with H3K4me1 are markers of active enhancer elements and are therefore expected to co-localize. A sampling of the p300 ChIP-Seq data shows the expected co-localization of p300 and H3K4me1." (https://www.activemotif.com/catalog/details/61401).
RNAP2 antibody was validate by the manufacturer: "RNA pol II antibody (mAb) tested by ChIP-Seq.
ChIP was performed using the ChIP-IT® High Sensitivity Kit (Cat. No. 53040) with chromatin from 2.3 million HL-60 cells and 20 ul of antibody. ChIP DNA was sequenced on the Illumina HiSeq and 30 million sequence tags were mapped to identify Pol II binding. ChIP-Seq data from three specific genes is shown as an example. Pol II binding is detected at the 5´ end of the genes, throughout the gene bodies and at the 3´ end of the genes." (https://www.activemotif.com/catalog/details/39097/rna-pol-ii-antibody-mab)
SUZ12 antibody was validated in: Zhang W et al. The BAF and PRC2 Complex Subunits Dpf2 and Eed Antagonistically Converge on Tbx3 to Control ESC Differentiation. Cell Stem Cell 24:138-152.e8 (2019).
CBX7 antibody was validated in: Fursova NA et al. Synergy between Variant PRC1 Complexes Defines Polycomb-Mediated Gene Repression. Mol Cell 74:1020-1036.e8 (2019).
PHC1 antibody was validated in: Blackledge NP et al. PRC1 Catalytic Activity Is Central to Polycomb System Function. Mol Cell. (4)857-874 (2020).
GATA6 antibody was validated in: Molotkov et al. Distinct Requirements for FGFR1 and FGFR2 in Primitive Endoderm Development and Exit from Pluripotency. Dev. Cell, 2017;0(0).
SOX1 antibody was validated in: Lager et al. Rapid functional genetics of the oligodendrocyte lineage using pluripotent stem cells. Nat Commun, 2018;9(1):3708.
Donkey anti-Goat igG Alexa FLuor Plus 488 and Donkey anti-Goat igG Alexa FLuor Plus 596 were validated in: Cruz-Molina, S. et al. PRC2 Facilitates the Regulatory Topology Required for Poised Enhancer Function during Pluripotent Stem Cell Differentiation. Cell Stem Cell 20, 1–17 (2017).

## Eukaryotic cell lines

Policy information about cell lines

| | |
|---|---|
| Cell line source(s) | Male mouse ESC line E14Tg2a was used for all experiments. This cell line was a kind gift from Joanna Wysocka´s lab (Standford University). |
| Authentication | The insertions, deletions and inversions were authenticated by PCR genotyping and confirmed by Sanger-sequencing. |
| Mycoplasma contamination | Both WT E14 mESC and all the transgenic ESC lines tested negative for mycoplasma contamination. |
| Commonly misidentified lines (See ICLAC register) | None |